CONSTRUCTION OF A PULSING SYSTEM FOR LOW-ENERGY POSITRONS

Antti Laakso

Laboratory of Physics
Helsinki University of Technology
Espoo, Finland

Dissertation for the degree of Doctor of Science in Technology to be presented with due permission of the Department of Engineering Physics and Mathematics, Helsinki University of Technology for public examination and debate in Auditorium K at Helsinki University of Technology (Espoo, Finland) on the 29th of June, 2005, at 13 o'clock.

Dissertations of Laboratory of Physics, Helsinki University of Technology
ISSN 1455-1802

Dissertation 133 (2005):
Antti Laakso: Construction of a pulsing system for low-energy positrons
ISBN 951-22-7745-X (print)
ISBN 951-22-7746-8 (electronic)

Abstract

Positron lifetime spectroscopy is a powerful tool to identify vacancy type defects in semiconductor materials. Conventionally, applicability of the positron lifetime measurement has been limited to bulk samples. However, many interesting materials are nowadays available only as thin epitaxial samples. In order to measure these samples a positron lifetime beam is needed.

This work describes the concept and the design of a pulsed low-energy positron lifetime beam facility. The theoretical background of the beam pulsing is reviewed. The construction of the pulsing system is presented in detail and results from electron and positron tests with this beam facility are introduced. As an application of the pulsed lifetime beam the results of the measurements on InN layers done at Universität der Bundeswehr are also presented.

The pulsing system in this work is composed of three different components, two bunchers and a chopper. The bunchers modulate the beam velocity to create a time varying positron beam intensity and to result a very narrow positron bunch at the target. The chopper is used to get rid of the background between the pulses and to improve the peak to background ratio. When this pulsing system is tested with electrons, a full width at half maximum of 160 ps and a peak to background ratio of 5000:1 is obtained. For positrons, the values are 270 ps and 4000:1 respectively.

Preface

This thesis has been prepared in the Laboratory of Physics at the Helsinki University of Technology during the years 1998 – 2005. I wish to thank my supervisor Professor Pekka Hautojärvi for the opportunity to work at the Laboratory and also guidance and support.

I express gratitude to Professor Kimmo Saarinen for advising this thesis, especially on questions related to semiconductor and positron physics.

In addition, I have had many good colleagues at the Laboratory of Physics. First, I want to thank Antti Pelli and Floris Reurings for being great collaborators in the pulsed beam project. Also, the discussions on the technical things with Dr. Klaus Rytsölä are appreciated. The technical support from Mr. Heikki Vaalte and Mr. Kaarle Tahvanainen is invaluable. There are also numerous other people in the laboratory, both in experimental and computational group, who all deserve thanks.

On the family side, I want to thank my family, and especially my parents-in-law for the support when I was writing the last parts of the thesis.

Finally, my warmest thanks goes to my beloved wife Heli for all the great things that we've had during the years.

Helsinki, June 2005

Antti Laakso

Contents

List of Publications

[I] A.Laakso, K. Saarinen, and P. Hautojärvi. Positron lifetime beam for defect studies in thin epitaxial semiconductor structures. *Physica B*, 308-310:1157–1160, 2002.

[II] A.Laakso, M. Hakala, A. Pelli, K. Rytsölä, and K. Saarinen. Computer simulations of the scattering effects in a positron lifetime beam line. *Material Science Forum*, 445-446:489–491, 2004.

[III] F. Reurings, A. Laakso, K. Rytsölä, A. Pelli, and K. Saarinen. Compact positron beam for measurement of transmission moderator efficiencies and positron yields of encapsulated sources. *Accepted for publication in Applied Surface Science*, 2005.

[IV] A. Pelli, A. Laakso, K. Rytsölä, and K. Saarinen. High voltage design of a positron lifetime beam with groundend sample. *Material Science Forum*, 445-446:504–506, 2004.

[V] A. Laakso, A. Pelli, K. Rytsölä, K. Saarinen, and P. Hautojärvi. Determination of the timing properties of the pulsed positron lifetime beam by the application of an electron gun and a fast microchannel plate. *Accepted for publication in Applied Surface Science*, 2005.

[VI] J. Oila, A. Kemppinen, A. Laakso, K. Saarinen, W. Egger, L. Liszkay, P. Sperr, H. Lu, and W. J. Schaff. Influence of layer thickness on the formation of In vacancies in InN grown by molecular beam epitaxy. *Applied Physics Letters*, 84:1486–1489, 2004.

[VII] A. Laakso, J. Oila, A. Kemppinen, K. Saarinen, W. Egger, L. Liszkay, P. Sperr, H. Lu, and W. J. Schaff. Vacancy defects in epitaxial InN: identification and electrical properties. *Journal of Crystal Growth*, 269:41–49, 2004.

This thesis consists of these publications and this introductory overview.

The author's contribution

The author has had an active role in all phases of the work reported in this thesis. The author has written the publications [I, II, V, VII]. He has also had significant role in the designing and testing of the constructions presented in publications [III, IV]. He has been responsible for the positron lifetime measurements and data analysis of the publication [VI].

In addition to these publications, the author has been responsible for the design, construction and the testing of the pulsing system in years 1999 – 2004. The pulsed positron lifetime beam project has been largely collaborative work and more than ten people have contributed to this project by a varying degree. It should be noted that part of the designs and developments have been already published earlier, especially the original idea and the concept of the beam by K. Fallström [1].

1 Introduction

Positron spectroscopy is a method for the direct identification of vacancy defects [2]. It is based on monitoring the 511 keV annihilation radiation emitted when thermalized positrons annihilate in solids with electrons. Positrons get trapped at neutral and negative vacancies because of the missing positive charge of the ion cores. At vacancies, the positron lifetime increases and positron-electron momentum distribution narrows due to reduced electron density.

The spectroscopy gives information on vacancies at concentrations $10^{15} - 10^{19}$ cm^{-3}. Positron lifetime is a direct measure of the open volume of a defect. The Doppler broadening of the 511 keV radiation gives the momentum distribution of annihilating electrons $\rho_{\mathrm{v}}(p)$. The core electron momentum distribution can be used to identify the sublattice and impurity surroundings of a vacancy. In addition, under varying temperature and illumination, the positron spectroscopy can yield information on charge states, optical transitions and thermal stabilities of vacancy defects.

The lifetime and Doppler broadening are easily applied to bulk samples. Thin epitaxial semiconductor layers can also be studied by Doppler broadening spectroscopy using a positron beam. However, positron lifetime spectroscopy, which is essential for obtaining the open volume of a defect, has been mainly limited to bulk samples and until now only two pulsed positron beam facilities utilizing similar principles as in this work have been constructed and are operational, one in Munich, Germany and other in Tsukuba, Japan [3, 4].

In this work we first give a short introduction to positron annihilation spectroscopy and motivate the need for a pulsed positron lifetime beam in chapter 2 and publication [I]. The concept of a pulsed positron beam and the theoretical background is briefly presented in chapter 2. The technical implementation of the pulsed beam is introduced in chapter 3 and in publications [II, III, IV, V]. The results of the tests with the constructed beam are presented in chapter 4 and publication [V]. The pulsed positron beam was applied to study vacancy defects in InN (chapter 5 and publications [VI, VII]). In these studies, the lifetime setup of Universität der Bundeswehr was utilized.

2 Methods and background

2.1 Conventional positron techniques

In conventional positron lifetime spectroscopy (see Fig. 1) a positron mean lifetime is extracted from a distribution of observed time differences of 1.28 MeV photons emitted in β^+ decay and the 511 keV photons emitted when electron-positron pair annihilates. The positron lifetime spectrum is composed of exponential decay components with intensities I_i and lifetimes τ_i as $\sum_i I_i e^{-t/\tau_i}$. The different exponential components are associated to annihilations at different positron states (bulk vs. vacancy). This spectrum can be relatively easily decomposed and the individual lifetimes and their intensities can be extracted.

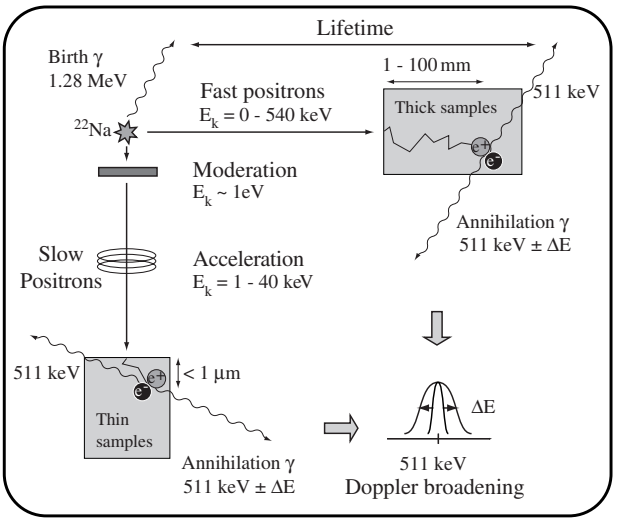

Figure 1. *The principle of the positron experiment. Sources and measurable quantities.*

As an example, two different lifetime spectra from undoped and highly Mg-doped GaN bulk samples are shown in the Fig. 2. In the highly Mg-doped sample only one lifetime component of 165±1 ps can be observed. However, in the undoped sample a second lifetime component of 235±5 ps is present. This second component is due to Ga vacancies existing as native defects in n-type GaN. The intensity of the second component gives an estimate of the vacancy concentration (10^{17} cm^{-3} in this case).

The average lifetime τ_{av} is defined as the center-of-mass of the lifetime spectrum,

$$\tau_{\mathrm{av}} = (1 - \eta_v)\,\tau_{\mathrm{B}} + \eta_v \tau_{\mathrm{V}} = \mathrm{C.M.}, \tag{1}$$

where η_{V} is the fraction of the positrons annihilating in the vacancies and τ_{B} and τ_{V} are the bulk and vacancy lifetime, respectively. It should be noted that τ_{av} is a statistically accurate parameter and its changes below 1 ps can be measured.

In Doppler broadening experiments the momentum distribution of the annihilating electrons is recorded by measuring the Doppler shift ΔE of the annihilation radiation with a Ge-detector. The momentum distribution $\rho(p)$can be characterized by integrated S- and W-parameters shown in the Fig. 3. The measured momentum distribution $\rho\,(p)$ is composed of the superimposed distributions from annihilations in vacancies $\rho_{\mathrm{V}}\,(p)$ and in bulk $\rho_{\mathrm{B}}\,(p)$ as shown in Eq. 2,

$$\rho\,(p) = (1 - \eta_v)\,\rho_{\mathrm{B}}\,(p) + \eta_v \rho_{\mathrm{V}}\,(p)\,. \tag{2}$$

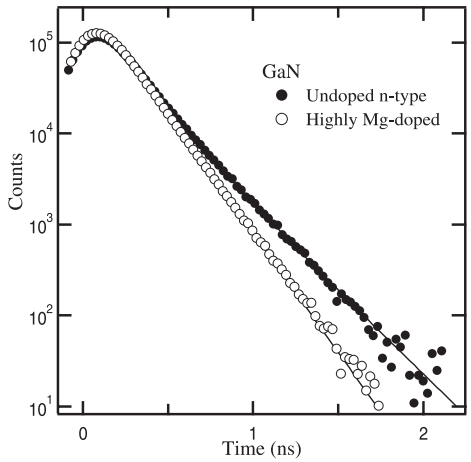

Figure 2. *Positron lifetime spectra from two different GaN bulk samples. In the highly Mg-doped sample (white circles) only one lifetime component of 165 ps is present. In the undoped n-type sample a longer lifetime component of 235 ps is present due to vacancies. Resolution of the system is 220 ps (FWHM) and the slope of the prompt is 40 ps. [5].*

Very often this can not be decomposed on its own. However, decomposition is possible, if the annihilation fraction η_V and the bulk momentum distribution $\rho_B(p)$, determined by measuring a defect free reference sample, is known.

In practice, identification of the vacancies is based on measuring both τ_V and $\rho_V(p)$. τ_V is obtained from decomposition of the lifetime spectra and it can be used to determine $\rho_V(p)$ (Eqs. 1–2). This means that the lifetime measurement is normally needed for identification of the vacancies. Furthermore, positron lifetime spectroscopy is approximately ten times more sensitive to defects than Doppler broadening spectroscopy.

In the conventional fast positron experiment the positrons are emitted directly from ^{22}Na source and are implanted to the sample. These positrons have continuous energy range from 0 up to 540 keV and a wide stopping profile ranging up to 100 μm. Thus, bulk samples with dimensions of 5 mm$\times$5 mm and thickness $> 100\mu$m are needed.

In principle, low energy positrons needed in slow positron experiment can be obtained by filtering out fast positrons emitted from the ^{22}Na source by an energy selector in the positron beam. However, the slow positron - fast positron ratio of a ^{22}Na source is poor and therefore a moderator is needed. The moderator, eg. single crystalline W foil, is placed in front of the source and fraction of the fast positrons will thermalize in the moderator crystal . These thermal positrons are emitted from the surface of the moderator due to the negative work function for positrons (energies less than 1 eV) and the slow positron - fast positron ratio will increase significantly compared to an unmoderated case. These nearly monoenergetic slow positrons can then be separated from the remaining fast positrons with an energy filter and further accelerated in an adjustable electric field to energies up to 60 keV in order to study layers with thicknesses of 0 – 5 μm. [6]

Both lifetime and Doppler broadening measurements can be done routinely with fast positrons. On the other hand, slow positron beam experiments are mainly limited to Doppler broadening measurements. This is because the time information of the positron's entrance to the sample is lost in the beam formation. However, a low-energy pulsed positron beam enables the lifetime measurements in thin layers.

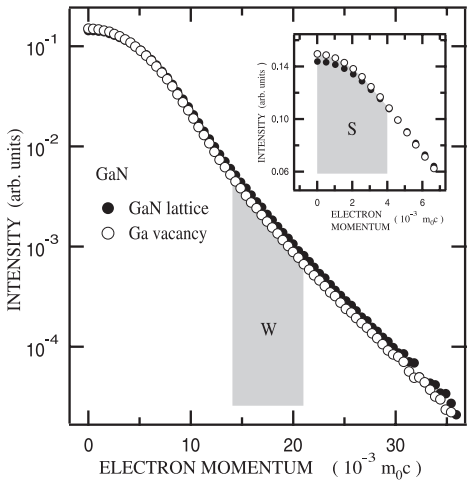

Figure 3. *Area normalized momentum distribution of annihilating electrons measured in Doppler broadening experiment. The S- and W-parameters, which are commonly used to describe the line shape, are defined as integrals over the shaded areas.*

2.2 Methods for slow positron lifetime experiments

Several methods to perform lifetime measurements with a slow positron beam have been introduced [7–10]. The general problem that needs to be solved is the question, how to obtain the start signal for the lifetime measurement, as the detection of the 1.28 MeV birth photon and the annihilation photons is not applicable. The reason for this is the unequal number of the start signals compared to the stop signals, since only very few positrons, less than one in 10^4, survive the moderation process and reach the sample.

Successful methods are based either on the detection of the secondary electrons generated on the implantation of the positron into the sample or the pulsing of the beam. The first method utilizes a channeltron or a microchannel plate as a timing detector for the secondary electrons. The resolution with these methods is rather poor, in the range of 350 ps to 1000 ps. Several beams have been realized especially for polymer studies [11–13].

The most successful method leading to the best time resolution is based on the beam pulsing. In this technique one tries to control precisely the time instant when the positron enters the sample and uses this predefined information for the lifetime measurement. In practice, this method means that the continuous beam is pulsed in an appropriate way.

Several methods to accomplish this have been introduced. One is based on applying instantaneously a longitudinal harmonic potential on the incoming beam. The harmonic potential accelerates the late coming positrons more compared to the earlier ones so that all the positrons under the harmonic field arrive simultaneously to the target [9, 14, 15].

Another alternative is to trap the moderated positrons into a Penning trap (a magnetic bottle) and extract them by a time varying potential. This technique has advantages if the positrons can be cooled in the trap - the energy spread of the extracted beam can be small, even 18 meV [16]. In addition, highly effective (efficiencies up to 10^{-2} with solid Ne moderator) solid rare gas moderation can be utilized, since the cooling improves the beam brightness over the initially large momentum spread of the rare gas moderation. The initial pulse having duration of 18 ns can be further compressed by a subsequent buncher and the time resolutions adequate for semiconductor applications should be reachable [16–19].

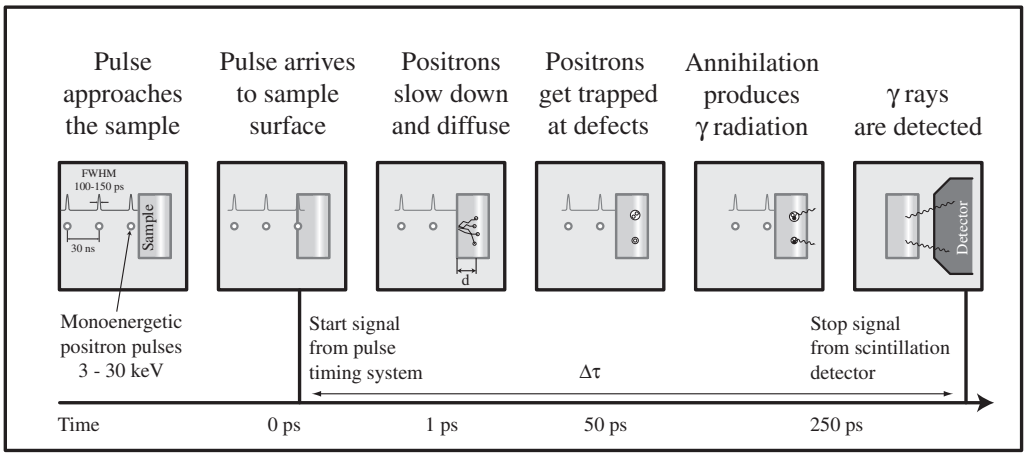

Figure 4. *Simplified idea of the timing principle of the pulsed positron lifetime beam.*

Probably the most successful beam pulsing technique is based on RF-pulsing of the initially continuous slow positron beam. The ideas of this method are largely derived from the heavy-ion and the electron pulsing and bunching systems [20–23]. In this method the beam is chopped and/or bunched with a high frequency electric fields to yield narrow positron pulses with a full width at half maximum (FWHM) of 200 ps or less with well defined time structure. The principle of the lifetime measurement in this system is shown in Fig. 4. The positron lifetime can be understood as the difference of the time when the positron pulse enters the sample and the time when the positron annihilates with the electron. In practice, the annihilation signal is used to start the lifetime measurement and the first clock pulse from the pulsing electronics following the start is used to stop the measurement.

Beams utilizing this principle have been successfully realized in München, Germany and Tsukuba, Japan [7, 10, 24]. The pulsed positron lifetime beam at the Helsinki University of Technology, discussed in this work, is also based on this technique. Several other attempts to construct a pulsed beam with a time resolution suitable for polymer studies (i.e. FWHM's of 300 ps to 2.2 ns) have been reported [25–28].

2.3 Pulsed positron lifetime beam

2.3.1 Principle of beam timing by bunching and/or chopping

The initial problem of RF-pulsing is, how to create precisely timed, narrow positron pulses arriving at the target with a desired energy to enable the positron lifetime measurement. The pulse width should be of the order of the detector resolution, 100 – 200 ps for the annihilation photons. Repetition rate of the pulses should be stable, the period between pulses should be accurate within less than 25 ps over the time needed for the acquisition of one lifetime spectrum. Energy spread introduced in the beam by the velocity modulation should be small, so that the incoming pulse can be assumed nearly monoenergetic. Additionally, the beam intensity should be high enough to keep the time needed for the collection of one spectrum of $> 10^6$ counts acceptable (a few hours).

In principle, there are two possibilities to accomplish these goals: the bunching or the chopping of the beam. In the beam bunching, the longitudinal velocity of the continuous incoming beam is modulated to create periodical short pulses at the target as illustrated in Fig. 5. The advantage of this method is that no positrons are lost in the

modulation process and ideally all positrons from the initial beam can be 'compressed' to the pulses. Since the ideal bunching is not possible, a certain part of the positrons remains unbunched, creating a constant background between the pulses. In addition, the bunching process increases the energy spread of the beam. This can be a disadvantage if there is a need to implant monoenergetic low energy positrons to the sample.

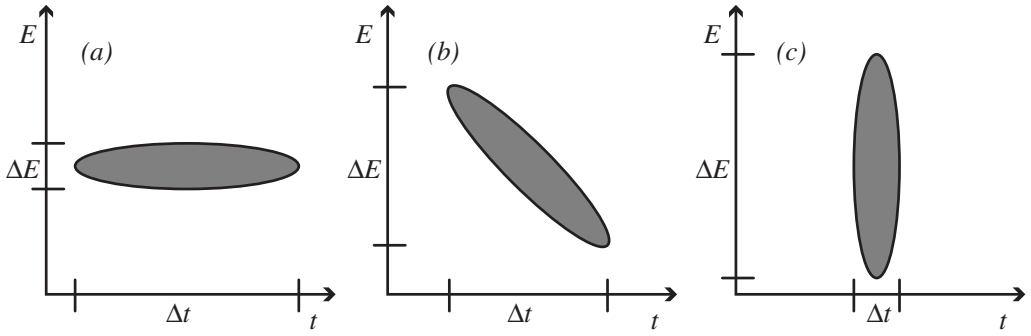

Figure 5. *Beam pulsing by bunching and the phase space conservation. (a) The time deviation of positron(pulse) is large before buncher. In the buncher the first positrons are slowed and the late coming accelerated and the phase-space volume starts to turn. (b) The energy spread increases and the time spread decreases. (c) In the target (time focus) the time spread reaches minimum and the energy spread is at maximum.*

Other alternative is to chop the beam. This means that the incoming continuous positron flux is periodically 'on' or 'off' and the velocity of the positrons in the beam is not modulated. By choosing a short enough time interval when the beam is 'on' it is possible to create very short pulses with the same energy as the initial continuous beam. Drawback of this method is the significant decrease of the beam intensity as most of the positrons are entering the chopper at its 'off' state.

To overcome the limitations of the chopping or bunching alone, both techniques are applied simultaneously. The buncher is used to compress the continuous beam to bunches increasing the beam intensity and the chopper is used get rid of the background due to the non-ideal bunching.

It is interesting to note the analogy of the pulsing of the beam to the optics or charged particle optics. The buncher is equivalent to an optical lens or a charged particle lens and can be thought as a 'time lens'. The chopper in turn is similar to an aperture or a collimator limiting the optical or charged particle beam diameter and it can be considered as a 'time width limiter'.

2.3.2 Beam bunching

Beam modulating waveform We shall now consider the beam bunching in more detail. In the following it is assumed that the beam is non-relativistic and the space charge effects can be neglected. Both these assumptions are valid for a low energy, low current positron beam.

Initially, there is a continuous beam with energy E_0 arriving to the buncher at a time interval $[-T_f/2, T_f/2]$, $T_f = 1/f$, where f is the base frequency of the beam pulsing system. The goal is to bunch the beam so that all the positrons arrive at the same time T at the target, located at the distance L from the buncher (the times and distances are illustrated in Fig. 6). The sum of the initial time t and the flight time $\tau(t)$ should equal to the flight time of an unmodulated particle τ_0 for all values of t,

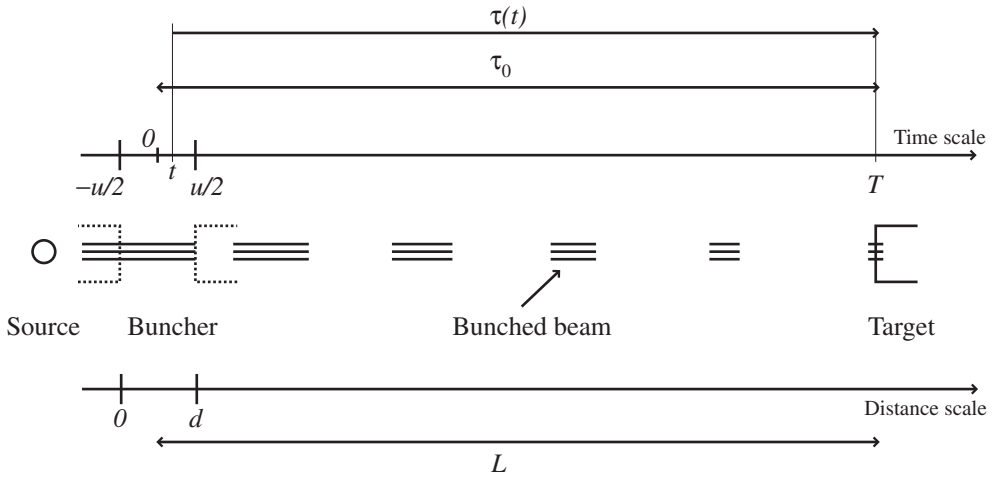

Figure 6. *The times and the distances used in bunching calculations. The time t is the instant at the buncher, $\tau(t)$ flight time from buncher to the target, τ_0 flight time for an unmodulated particle (constant), T time at the target, L the distance from the center of the buncher to the target and d the length of the buncher gap. u is the transit time through the bunching gap. Based on Ref. [20]*

$$t + \tau\left(t\right) = \tau_0,\ t \in [-T_f/2, T_f/2] \tag{3}$$

The flight time $\tau(t)$ is

$$\tau\left(t\right) = \frac{L}{v\left(t\right)}. \tag{4}$$

The simultaneous arrival of the positrons is achieved by modulating the longitudinal velocity $v(t)$. This is done by a time varying potential $U(t)$. The kinetic energy E_{mod} after the modulation is

$$E_{\mathrm{mod}}(t) = E_0 + E(t) = \frac{1}{2} m_e v_{\mathrm{mod}}^2\left(t\right),$$

where E_0 is initial energy and $E(t) = eU(t)$ the modulating component. This can be written as

$$v_{\mathrm{mod}}\left(t\right) = \sqrt{\frac{2(E_0 + E(t))}{m_e}}. \tag{5}$$

Combining 5 together with 3 and 4 we get

$$t + L\sqrt{\frac{m_e}{2\left(E_0 + E\left(t\right)\right)}} = \tau_0.$$

So

$$E\left(t\right) = \frac{m_e L^2}{2\tau_0^2} \frac{1}{\left(1 - \frac{t}{\tau_0}\right)^2} - E_0.$$

Then the general form for an ideal modulating potential is

$$U\left(t\right) = \frac{E_0}{e}\left(\frac{1}{\left(1 - t/\tau_0\right)^2} - 1\right). \tag{6}$$

This is the general ideal waveform for the beam bunching. However, it is very difficult to realize a buncher where the voltage varies parabolically when the bunching frequency is in the range of 10^7–10^8 Hz. In the lower frequencies of 10^6 Hz the parabolic bunching has been realized with inductive bunching [29, 30]. Deviations from the ideal bunching waveform always create background between pulses and thus a beam chopper is needed as discussed below.

The flight time from the buncher to the target is in practice long compared to the initial bunching period $t \ll \tau(t) \Rightarrow t \ll \tau_0$ which yields the simplification of Eq. 6

$$U\left(t\right) \approx \frac{E_0}{e}\left(\frac{1}{\left(1-2t/\tau_0\right)}-1\right) \approx \frac{2E_0}{\tau_0 e}t. \tag{7}$$

This means that the optimal modulating potential is a sawtooth (a repeated voltage ramp) wave. However, it is challenging to create an ideal sawtooth wave in the buncher with adequate amplitude when the base frequency is in the 10^8 Hz range. Thus, the buncher is often realized as a simple, single frequency resonator and the sawtooth is approximated by a sinewave $U(t) = U_0 \sin(\omega t)$, which yields optimal waveform only at the vicinity of the zero-crossing. The Eq. 7 can be thus written as

$$U_0 \sin\left(\omega t\right) \approx U_0 \omega t = \frac{2E_0}{\tau_0 e}t.$$

Then we get

$$U_0 = \frac{2E_0}{\tau_0 e \omega} = \frac{2}{e\sqrt{m_e}}\frac{\sqrt{2E_0^3}}{\omega L}.$$

This can be used to approximate the voltages and frequencies needed in the beam bunching, and the lengths of the drift tubes.

Beam intensity as a function of time The beam intensity before the the buncher $I_0(t) = I_0$ is constant. The intensity after the buncher at an observation point is denoted as $I(t)$. When we bunch the time interval dt of the beam and observe it at later point as dT, then the charge conservation requires

$$I_0 dt = I(t) dT.$$

From this we get

$$I(t) = I_0\left(\frac{dT}{dt}\right)^{-1} = I_0 T'(t)^{-1}.$$

Thus, we need to know $T'(t)$ in order to know $I(t)$ as a function of time.

The arrival time of a bunched particle at the observation point (target) can be written as $T(t)$:

$$T(t) = t + \frac{L}{v(t)}, \tag{8}$$

where t is the time when a positron crosses the buncher, L is the distance from the buncher to the target and $v(t)$ is the velocity of the particle when it exits the buncher. The velocity depends on the kinetic energy and Eq. 5 can be approximated by

$$v_{\mathrm{mod}}(t) = \sqrt{\frac{2E_0}{m_e}}\left(1+\frac{eU(t)}{E_0}\right)^{1/2} \approx v_0\left(1+\frac{1}{2}\frac{eU(t)}{E_0}\right). \tag{9}$$

Here, v_0 denotes the initial beam velocity and it has been assumed that $eU(t) \ll E_0$. From Eq. 8 and Eq. 9 we get for the arrival time

$$T(t) = t + \frac{L}{v_0} \frac{1}{1 + \frac{1}{2}\frac{eU(t)}{E_0}}. \tag{10}$$

If the ratio L/v_0 is denoted as τ_0, the unmodulated flight time from the buncher to the target, then Eq. 10 is further approximated ($eU(t) \ll E_0$) as

$$T(t) = t + \tau_0 \left(1 - \frac{1}{2}\frac{eU(t)}{E_0}\right). \tag{11}$$

From this we get for the time derivative $T'(t)$

$$T'(t) = 1 - \tau_0 \frac{1}{2}\frac{e}{E_0}\frac{dU(t)}{dt} \tag{12}$$

and the beam current is then

$$I(t) = \frac{I_0}{1 - \tau_0 \frac{1}{2}\frac{e}{E_0}\frac{dU(t)}{dt}}\ . \tag{13}$$

We now define the dimensionless bunching parameter χ, which is used to describe the time focusing properties of the buncher and to simplify equations in the following. The bunching parameter,

$$\chi = \left(\frac{\omega L}{v_0}\right)\left(\frac{eU_0}{2E_0}\beta\right),$$

can be considered as a normalized distance from the buncher to the time focus. It is very useful when the beam parameters are estimated or when the test results are analyzed. Commonly, the dimensionless transit time factor β is added to the expression of χ. It describes how much the buncher gap voltage changes when the positron passes through the gap. This parameter takes into account the time u that is needed to pass through the buncher gap length d, see Fig. 6. For a sinewave modulation, β can written as [20,22]

$$\beta = \frac{\sin(\omega d/(2v_0))}{\omega d/(2v_0} \leq 1.$$

The value of β is in our beam unity with a very good accuracy and therefore it is neglected in the following derivations and only briefly reviewed when the aberrations are discussed.

When the bunching waveform is sawtooth-like, $U(t) = U_0\omega t$, we get

$$T_{\mathrm{saw}}(t) = t + \tau_0 \left(1 - \frac{1}{2}\frac{eU_0}{E_0}\omega t\right) = t + \tau_0 - \chi t \tag{14}$$

$$T'_{\mathrm{saw}}(t) = 1 - \tau_0 \frac{1}{2}\frac{eU_0}{E_0}\omega = 1 - \chi \tag{15}$$

$$I_{\mathrm{saw}}(t) = \frac{I_0}{1 - \tau_0 \frac{1}{2}\frac{eU_0\omega}{E_0}} = \frac{I_0}{1-\chi}\ . \tag{16}$$

With sinusoidial bunching $U(t) = U_0 \sin\omega t$, the time derivative and current read as

$$T_{\sin}(t) = t + \tau_0 \left(1 - \frac{1}{2}\frac{eU_0}{E_0}\sin\omega t\right) = t + \tau_0 - \frac{\chi}{\omega}\sin\omega t \tag{17}$$

$$T'_{\sin}(t) = 1 - \tau_0 \frac{1}{2}\frac{eU_0}{E_0}\omega\cos\omega t = 1 - \chi\cos\omega t \tag{18}$$

$$I_{\sin}(t) = \frac{I_0}{1 - \tau_0 \frac{1}{2}\frac{eU_0\omega\cos\omega t}{E_0}} = \frac{I_0}{1-\chi\cos\omega t}. \tag{19}$$

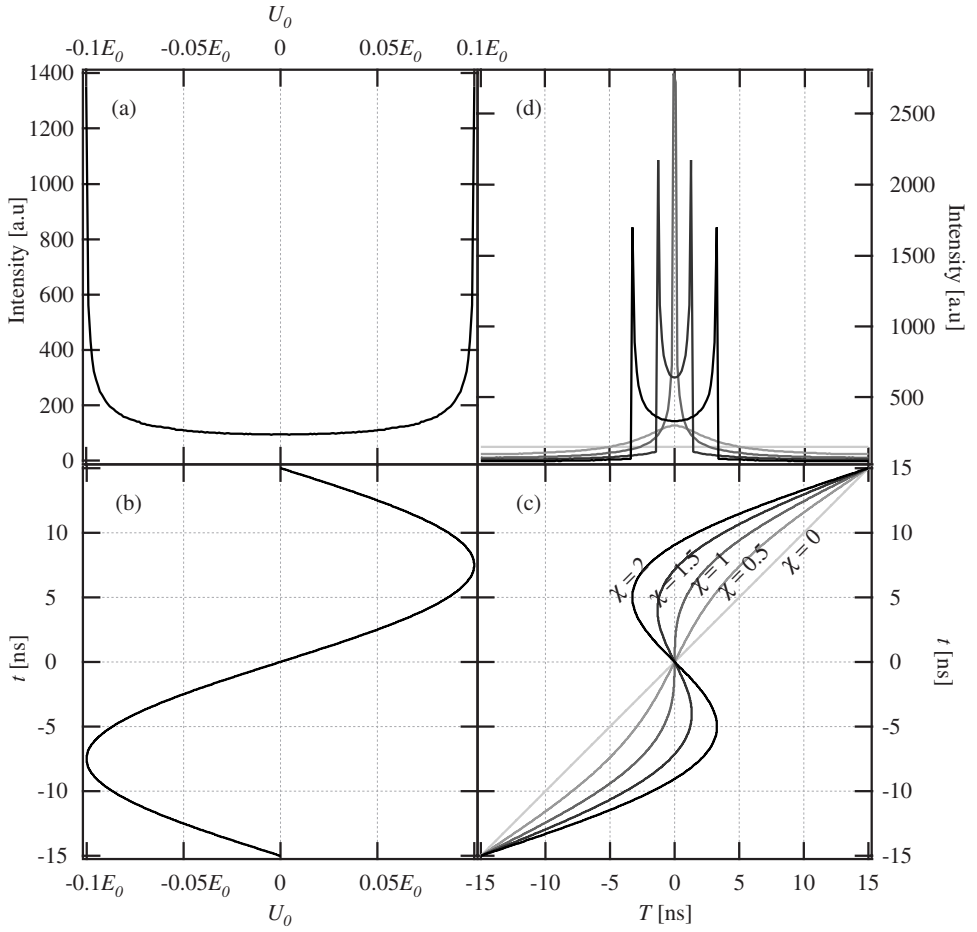

Figure 7. *The bunch evolution for different values of χ in sinusoidial bunching. In this case a base period of 30 ns was used with a modulation voltage of $U_0 = 0.1E_0$. (a) The distribution of the bunching waveform energy,(b) the bunching voltage vs. time. (c) Phase plot of initial period t vs. the arrival time T, the unmodulated flight time τ_0 has been subtracted from times T. (d) The corresponding intensity distribution $I(T)$.*

It is readily seen from Eq. 16 and Eq. 19 that when χ approaches one, the current I increases and at the value $\chi = 1$ time focus is reached and maximum bunching is obtained. The intensity distribution, (t, T)-phase space (time t at the buncher vs. time T at the target), the voltage of the bunching waveform vs. the bunching time and the voltage distribution of the waveform for the sinusoidal bunching are illustrated in Fig. 7. It can be seen from this figure (plot (d) that some background will remain in the final intensity distribution (timing spectrum). This means also that the efficiency of the simple sinewave buncher is always less than 1 and only part of the positrons get bunched to the pulse and the rest remain in the background. To get rid of this background a beam chopper is needed.

The buncher can also be supplied with a second (or higher order) harmonic in order to mimic the sawtooth (ramp) waveform. This is commonly called harmonic bunching and in the case of f and $2f$-components the bunching voltage can be written as $U(t) =$

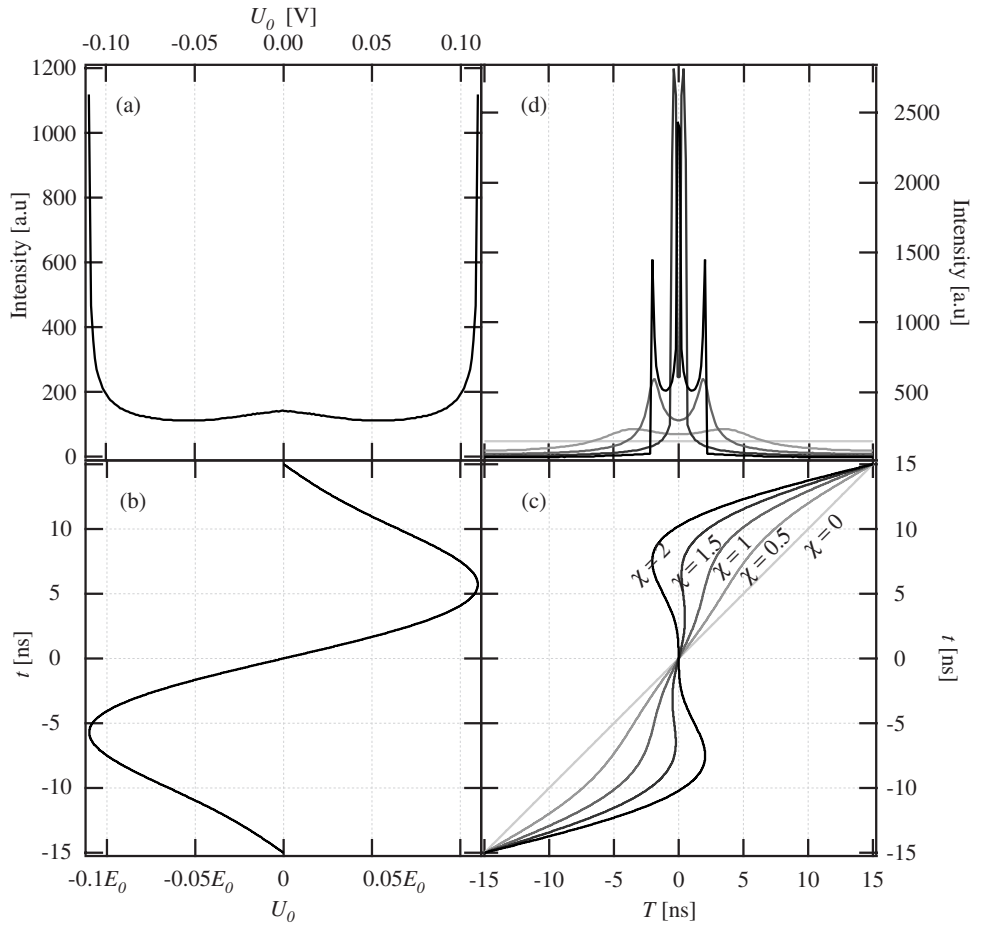

Figure 8. *The bunch evolution for different values of χ when using harmonic bunching. In this case the modulating voltage is of the form $U_0 \sin\omega t + 0.25U_0 \sin 2\omega t$ and the other parameters are as in Fig.7. It can be seen that the introduction of the second harmonic improves the efficiency of the buncher. The plots (a) – (d) correspond to those in Fig. 7.*

$U_0 \sin\omega t + AU_0 \sin 2\omega t$ and the following equations apply:

$$T_{2\mathrm{f}}(t) = = t + \tau_0 - \frac{\chi}{\omega}\left(\sin\omega t + A sin 2\omega t\right), \tag{20}$$

$$T'_{2\mathrm{f}}(t) = 1 - \chi\left(\cos\omega t + A\cos 2\omega t\right), \tag{21}$$

$$I_{2\mathrm{f}}(t) = \frac{I_0}{1 - \chi\left(\cos\omega t - A\cos 2\omega t\right)}. \tag{22}$$

The corresponding intensity distribution, (T, t)-phase space, the voltage of the bunching waveform vs. bunching time and the voltage distribution of the waveform are shown Fig. 8. By comparing the phase space plot shown in Fig. 8 (c) to the simple sinewave bunching shown in Fig.7 (c) it can be noticed that there is more 'wiggling' around zero ($T = 0$) in the case of harmonic bunching meaning better bunching efficiency vs. bunch width.

2.3.3 Bunch spread due to aberrations

Time spread of the bunch From the Liouville theorem follows that the phase volume of the beam is constant under the presence of conservative forces. This means that in an ideal system the final bunch width is determined only by the initial momentum spread of the positron source. However, real beams and bunchers provide bunches with finite widths due to different aberrations. Some of these aberrations result from the bunching process itself, some are from the beam transport and some can originate from the interaction of the beam and the buncher. The two latter can be thought to be originating from irreversible mixing of momentum components (longitudinal vs. transversal) in the phase space under the influence of the conservative forces in the different parts of the beam. In this case the phase volume stays constant but the shape of the volume changes resulting an increased momentum spread in the longitudinal direction. [22]

Similarly, if there are any collisions (e.g. scatterings) in the beam then there are non-conservative forces acting on the beam which increase the phase volume of the beam and increase the longitudinal energy spread as well. The additional momentum spread due to the aberrations and the collisions sum up quadratically, resulting an ever-increasing longitudinal energy spread of a bunch. It should be noted that if the system is equipped with a remoderation stage, it is possible to compress the phase volume of the beam because of the non-conservative forces present in the slowing down of the positrons. The drawback is the loss of the beam intensity as many positrons are lost in the remoderation process. [14, 15, 22]

In the following the factors affecting the final bunch width are discussed in more detail. The first group of aberrations can be called spherical aberrations, which result from the non-ideal pulsing waveform. As discussed earlier the optimal parabolic bunching waveform is hard to obtain at high frequencies. When using the sinusoidal (or the harmonic) bunching, the deviation from ideal waveform limits the minimum attainable pulse width as well as the beam utilization and creates non-zero background in the time focus. The second group of aberrations is the chromatical aberrations resulting from the energy spread of the beam, e.g. the initial energy spread of the moderated positrons and the energy spread introduced to the beam due to non-idealities in pulsing components and accelerators. The third group of aberrations is the RF aberrations which are created in the pulsing components when the transit times through the bunching gaps vary depending on the diameter of the beam. Typically, the chromatical aberrations dominate the final bunch width and the two other affect it less. However, the bunching efficiency of the beam is related to the spherical aberrations and hence these aberrations are studied in more detail in the following.

Bunch spread due to spherical aberrations and the bunching efficiency When the beam is bunched with a sinewave voltage, the deviation from the ideal waveform introduces inherent time spread to the pulse at the time focus. This spread can be called spherical aberration and denoted with $\Delta\tau_s$. It is independent from the 'external' inaccuracies (the chromatical aberrations) like the energy spread of the incoming beam.

When the bunching is ideal, the whole period T_f of the incoming beam can be bunched and only the chromatical aberrations affect the final pulse width. However, with sinusoidial bunching one has to make a compromise between the bunching efficiency p (beam utilization factor) and the final bunch width. The additional bunch spread due to non-ideal bunching can the be estimated with $\Delta\tau_s$.

The bunching efficiency is defined as,

$$p = \frac{\Delta t}{T_f} = \frac{\omega \Delta t}{2\pi}, \tag{23}$$

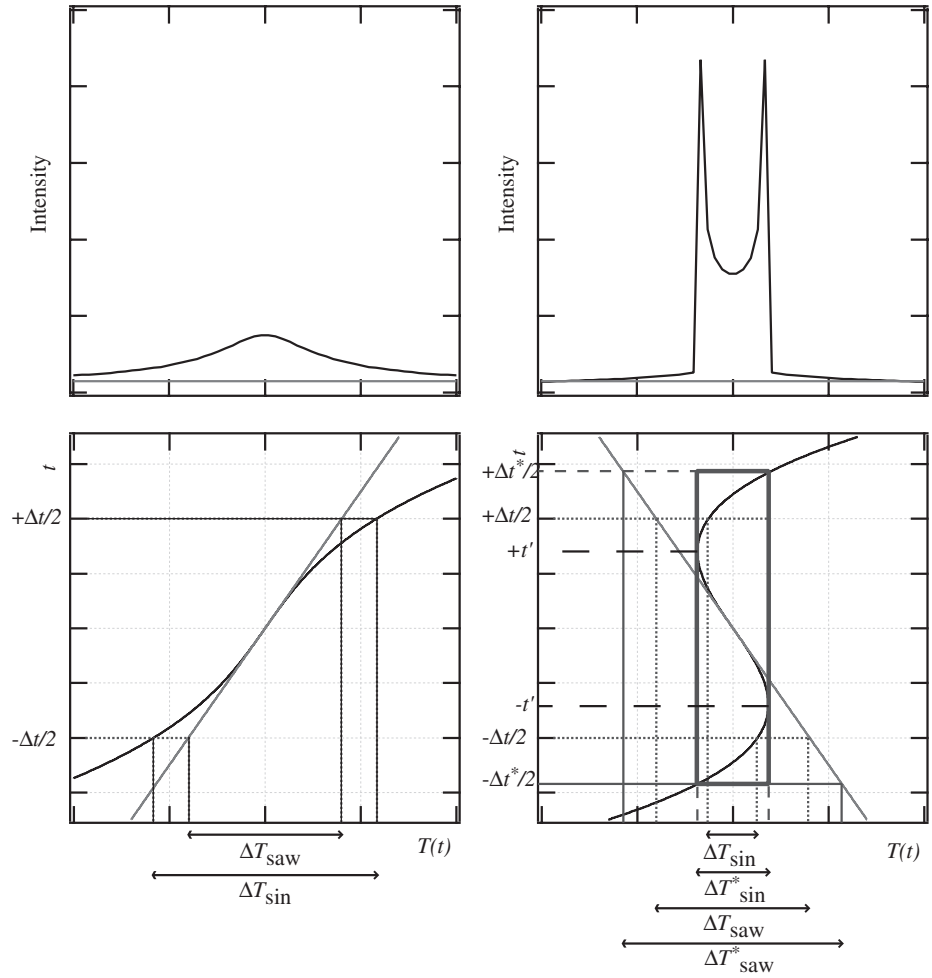

Figure 9. *The formation of spherical aberration due to non-ideal bunching waveform - a zoomed phase plot comparing a sinusoidally bunched beam to an ideally bunched sawtooth one. Left: underbunched beam with* $\chi = 0.8$*, right: overbunched beam with* $\chi = 1.2$*. Overbunching increases efficiency over sawtooth bunching.*

where Δt denotes the initial time width that is bunched to the final bunch. It should be noted that in practice p is determined with the chopper as described in section 2.3.4.

We now want to calculate the deviation from the ideal sawtooth (ramp) waveform (shown in the Fig. 9 on the left hand side) when the beam is underbunched $\chi < 1$.

Using Eq. 14 the pulse width at χ for ideal bunching is

$$\Delta T_{\mathrm{saw}} = T\left(\Delta t/2\right) - T\left(-\Delta t/2\right) = \Delta t - \tau_0 \frac{1}{2}\frac{eU_0}{E_0}\omega\Delta t = \Delta t\left(1-\chi\right). \tag{24}$$

Similarly for sinewave bunching we get from Eq. 17

$$\Delta T_{\mathrm{sin}} = \Delta t - \tau_0 \frac{1}{2}\frac{eU_0}{E_0}\left(\sin(\omega\Delta t/2) - \sin(-\omega\Delta t/2)\right) = \Delta t - 2\chi\frac{\sin(\omega\Delta t/2)}{\omega}\ .$$

This can further be approximated by using a series expansion

$$\Delta T_{\sin} = \Delta t - 2\chi\frac{1}{\omega}\left[\omega\frac{\Delta t}{2} - \frac{1}{6}\omega^3\left(\frac{\Delta t}{2}\right)^3\right] = \Delta t(1-\chi) + \frac{1}{24}\chi\omega^2\Delta t^3 \ . \qquad (25)$$

By comparing Eqs. 24 and 25 it becomes apparent that the spherical aberration is to first order

$$\Delta\tau_s = \chi\frac{1}{24}\omega^2\Delta t^3 = \chi\frac{1}{24}\omega^2\left(\frac{2\pi p}{\omega}\right)^3 = \chi\frac{\pi^3}{3}\frac{p^3}{\omega} \approx 10.3\frac{p^3}{\omega} \ . \qquad (26)$$

It can be clearly seen that by increasing the bunching efficiency p the spherical aberration increases drastically. To overcome this limitation of bunching efficiency vs. bunch width, several possibilities have been considered. The simplest way to improve efficiency while keeping the $\Delta\tau_s$ low, is to increase the bunching amplitude [7] and to overbunch the beam, which will be discussed later. Another alternative is to introduce harmonics to the bunching waveform, illustrated in Fig. 8 [31] and the third is to use a second sinusoidal buncher. If the second buncher is operating on a higher frequency than the first buncher, the combined effect is equal to the harmonic buncher. [32, 33]

The advantage of adding harmonics can be illustrated by considering a $2f$-harmonic buncher. For this we can calculate

$$\Delta T_{2f} = \Delta t - 2\chi\frac{\sin(\omega\Delta t/2)}{\omega} - 2\chi A\frac{\sin\omega\Delta t}{\omega} \ .$$

From a series expansion we obtain

$$\Delta T_{2f} = \Delta t(1-\chi) + \frac{1}{24}\chi\omega^2\Delta t^3 - 2A\chi\left(\Delta t - \frac{1}{6}\omega^2\Delta t^3\right) \ .$$

The last term presents the contribution of the second harmonic to the final pulse width and the two last terms can be used to estimate the relation between the spherical aberration and the bunching efficiency

$$\begin{aligned}\Delta\tau_{s,2f} &= \frac{1}{24}\chi\omega^2\Delta t^3 - 2A\chi\left(\Delta t - \frac{1}{6}\omega^2\Delta t^3\right) = \\ &= \chi\frac{\pi^3}{3}\frac{p^3}{\omega}(1+8A) - 4A\chi\pi\frac{p}{\omega} \ .\end{aligned}$$

The improvement of the efficiency of the $2f$-harmonic bunching over the sinusoidal bunching has been calculated numerically by Pandit et al. [31]. They show that the addition of the second harmonic component even with a small amplitude improves the bunching efficiency by 50 %.

We can now study ΔT when the beam is overbunched $\chi > 1$. This can be accomplished by increasing the drift distance or the bunching voltage amplitude or by decreasing the beam energy entering the buncher. The resulting time spectrum has two peaks, as seen in the Fig. 7 and Fig. 9, due to the faster particles passing by the slower ones. This yields a better efficiency and a shorter pulse width compared to the underbunched case. In the right hand side of the Fig. 9 the improved values for the overbunched pulse have been marked as Δt^* and ΔT^*. The ΔT^* can be calculated by first finding the values of t' for which the derivative $T'(t)$ vanishes, as seen in Fig. 7, and then using these values to find $\Delta T^*/2$. These values can be in turn used to find respective value of Δt by finding the solution for equations

$$\begin{aligned}-\Delta T^*/2 = \ & T(+t') = \ T(-\Delta t^*/2) \\ \Delta T^*/2 = \ & T(-t') = \ T(\Delta t^*/2)\end{aligned}$$

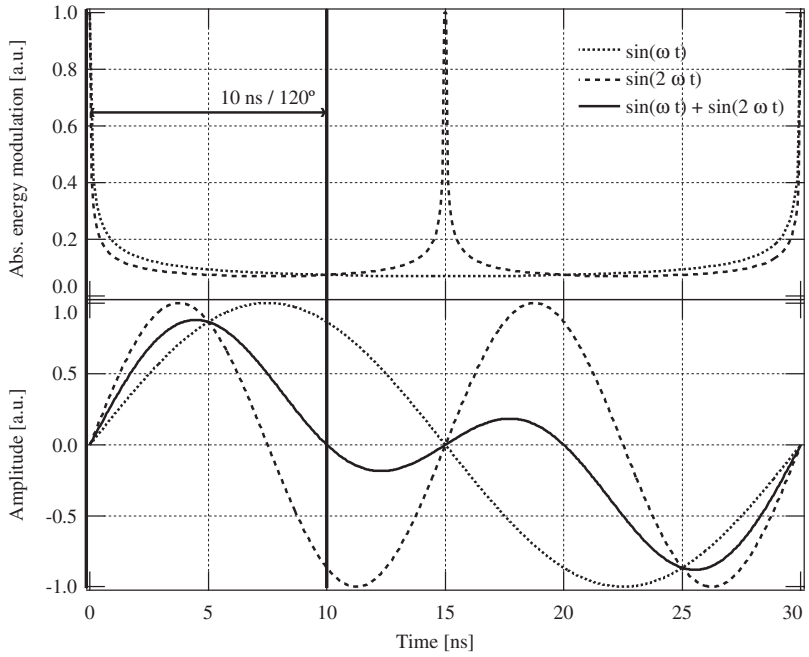

Figure 10. *The simplified idea of 120° 2f double gap prebuncher is to use the first gap to modulate the beam energy and choose the center electrode length so that the second gap does not modulate the beam. This is illustrated by plotting absolute energy modulation and the modulating voltage waveforms vs. the time (distance) from the first gap to illustrate the optimal length of 120° (or 240°) of the center electrode. In practice, the optimal energy modulation and bunch evolution of this buncher is very close to those shown in Fig. 8.*

or by the help of inverse function $t(T) = T^{-1}(t)$. Schödlbauer et al. [7] have shown that the relation between spherical aberration and the bunching efficiency is

$$\Delta\tau_s \approx \chi \frac{2\pi^3}{9\sqrt{3}} \frac{p^3}{\omega} \approx 4\chi \frac{p^3}{\omega}, \tag{27}$$

showing a significant improvement over the underbunched case of Eq. 26.

In our system we have combined all above mentioned possibilities to improve the bunching efficiency and to decrease the bunch width. The first buncher (later, the prebuncher), is a harmonic buncher operating on a base frequency f and on it's first harmonic $2f$. The second buncher (main buncher) is operating at $5f$ and with much higher voltage amplitude than the first one. The energy of the incoming beam to the main buncher is significantly larger than the energy modulation applied by the prebuncher so that both bunchers can be considered as independent bunchers. The prebuncher improves efficiency by collecting positrons to the chopping window (time focus at the chopper) and the main buncher provides the necessary time compression to reach the targeted bunch width.

The prebuncher is implemented as a double gap buncher where the center electrode is connected to the bunching voltage and the velocity modulation occurs in the gaps at both ends of the center electrode. The two harmonics in a double gap buncher necessitate the centre electrode length to be 120° of the period of the base frequency as illustrated in Fig. 10. [34]

The main buncher is realized as a simple sinewave double-gap buncher, where the energy modulation occurs in two short gaps between the grounded body of the buncher and the center electrode connected to the RF-voltage. Distance between the gaps is approximately 180° of the period so that the beam is exposed to bunching sinewave twice. Half period flight time between the gaps is so short that the pulse compression inside the buncher is negligible and thus the double gap buncher can be considered effectively as a simple single gap buncher. Technical details of this system will be discussed in chapter 3. [35]

Bunch spread due to chromatical aberrations Even though spherical aberrations produce microstructure to the final bunch time spectrum and cause spread compared to the ideal bunch, these effects are in practice small compared to the pulse spread due to chromatical aberrations in the system.

If the initial energy spread of the beam is denoted as ΔE_0, then the chromatical aberration $\Delta\tau_c$ is defined as

$$\Delta\tau_c = \frac{1}{2}\frac{\Delta E_0}{E_0}\tau_0 \ ,$$

where E_0 denotes the initial energy of the beam before entering the buncher and τ_0 is the unmodulated flight time from the buncher to the time focus. For example, we can calculate $\Delta\tau_c$ for the prebuncher when energy is 50 eV and the energy spread 2 eV and the flight time 200 ns then $\Delta\tau_c = 4$ ns. The bunch spreading due to energy spread in the initial beam is illustrated in Fig.11. It can be clearly seen that the spread smears the fine structure of the timing spectra.

This means that in order to achieve the final pulse width in the range of 100 ps the $\Delta E_0/E_0$ ratio for the main buncher must be small i.e. the beam energy E_0 should be large enough. However, considering the bunching parameter χ this requirement leads to the conclusion that the amplitude of the bunching waveform must be relatively high or the drift length to the target long in order to achieve proper compression of the pulse.

The main sources of the chromatical aberrations are the bunchers itself and to a lesser degree the different accelerating stages in the system. It has also been shown that the larger the beam diameter is, the larger the chromatical aberrations in the beam. [23, 36].

RF aberrations The RF-aberrations are due to the transit time spread in the bunchers. Depending on the radial distance from the center axis of the beam, the shape of the time dependent electric field in the bunchers changes and this results in changes in flight times through the chopper. This has been studied by Lynch et al. [23] and by Schödlbauer et al. [7]. They found that RF-aberrations are not significant if the buncher gap dimensions are small and the bunching frequency is not too high. In our case the RF-aberrations are largest at the main buncher but still negligible [36].

2.3.4 Beam chopping

The chopper is a relatively simple device the purpose of which is to let the beam pass through and to cut it out periodically. Mathematically it can be defined as

$$\begin{aligned} I(t) &= I(t), -rT_f/2 < t < rT_f/2, \quad 0 < r < 1 \\ I(t) &= 0, \quad \text{otherwise,} \end{aligned}$$

where T_f denotes the base period of the system and r the chopping time window.

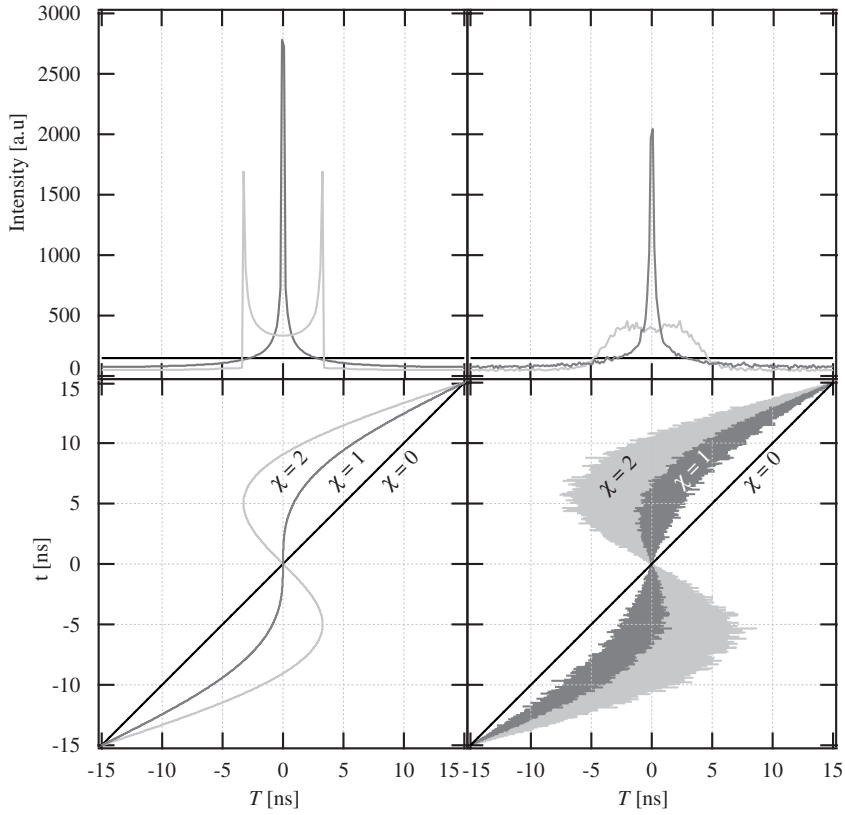

Figure 11. *The chromatical aberrations cause the broadening of the bunch illustrated by* (t, T)*-phase plot and the time histogram at the target plotted for three values of* χ*. On the left: the bunch evolution without the chromatical aberration. On the right: The bunch evolution when the relative energy spread* $\Delta E_0/E_0$ *is 0.15.*

Different concepts for beam chopping have been introduced. They can be divided into two categories, grid choppers and deflection choppers. The grid chopper can be implemented by using a set of grids perpendicular to the beam (resulting in an electric field parallel to the beam) directly in front of the source moderator or later in the beamline. A periodic voltage is applied to the source or grids and the periodically changing field creates the chopping action [4, 10, 28]. The challenge of this method is how to couple the square wave pulses necessary for the optimal chopping to the grids. It is difficult to make a wideband impedance match from the RF-amplifier to the grids, which can be considered as a simple lumped element capacitor. If the coupling is not good enough, the changes in the chopping field are not instantaneous due to the lack of higher frequency components and the chopper can introduce undesired longitudinal energy modulation to the beam. The other disadvantage is the increased energy spread in the magnetically guided beams due to the microlensing effects in the grid openings [37,38].

The other alternative, deflection chopper, uses a transversal electric field to increase the electron transversal velocity and the radius of the larmor precession in the magnetically guided beams. By placing a pair of electrodes in the beamline and applying a periodical voltage to them, a field perpendicular to the beam is created and the larmor radius of the positrons passing through this field is increased. With a slit or an aperture

placed to a proper position after the electrode, it is possible to cut out certain parts of the incoming beam and let the other parts pass through [1, 7, 24]. Properly designed deflection chopper does not introduce significant additional energy spread to the beam. In addition, the chopping field can be a simple sinusoidal waveform, which simplifies the system RF design.

It should also be noted that due to the finite dimension of the beam, the time profile of the deflection chopped beam is never rectangular but more like a gaussian, since the particles traveling away from the central axis get deflected and chopped easier than those traveling on the central axis. This can also reflect to the width of the time spectrum as discussed in chapter 4.

3 The design and construction of a pulsed positron lifetime beam facility

A schematical illustration of the pulsed positron beam facility in its final construction is shown in Fig. 12. The facility consists of the following parts: 1) the positron source, 2) the velocity selector to separate slow positrons from the fast positrons, 3) the prebuncher, 4) the drift tube, 5) the chopper and 6) the buncher. At the end of the beam the positrons are accelerated to the sample in the accelerator-decelerator 7) in the target chamber. The detector 8) is placed behind the sample. A Unique feature of this system is that the source and the pulsing system are floating at high voltage, (enclosed by the inner faraday cage, shown as shaded area in Fig. 12) and that the sample is grounded. The components of the beam and the electronics controlling them are described in more detail in the following sections. In Fig. 13 a photo of the beam is shown.

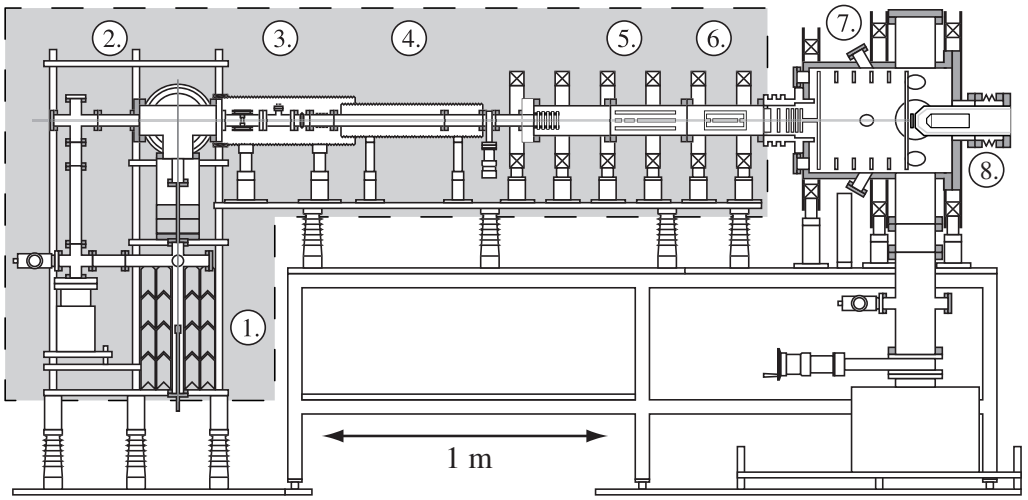

Figure 12. *The schematical drawing of the pulsed positron lifetime beam facility at the Helsinki University of Technology. 1. the source, 2. the velocity selector, 3. the prebuncher, 4. the drift tube, 5. the chopper, 6. the buncher, 7. the accelerator and decelerator, and 8. the detector. The inner and outer faraday cages shielding the beam are not shown.*

3.1 Slow positron beam generation

Beam generation Fast positrons are emitted from a ^{22}Na positron source (initial nominal activity 60 mCi at 04/2002, from iThemba labs, South-Africa), which is followed by a W(100) single crystal foil moderator (thickness 1 μm). The source and moderator holder, shown in Fig. 14 was designed to simplify the handling of the source and the moderator. The source is mounted to the end of a stainless steel rod that is supported by an insulating body of the source holder made of polyoxymethylene, POM (also known as polyacetal or Delrin). The steel rod also acts as a conductor to bring the bias voltage to the source. The moderator holder is attached to this rod with a M22×1 thread.

The moderator is placed between two circular tantalum frames and these frames are point welded together. This moderator package is mounted on top of the moderator holder and is kept on place by a stainless steel cap locked into the moderator holder by two screws tightened to a wedge groove.

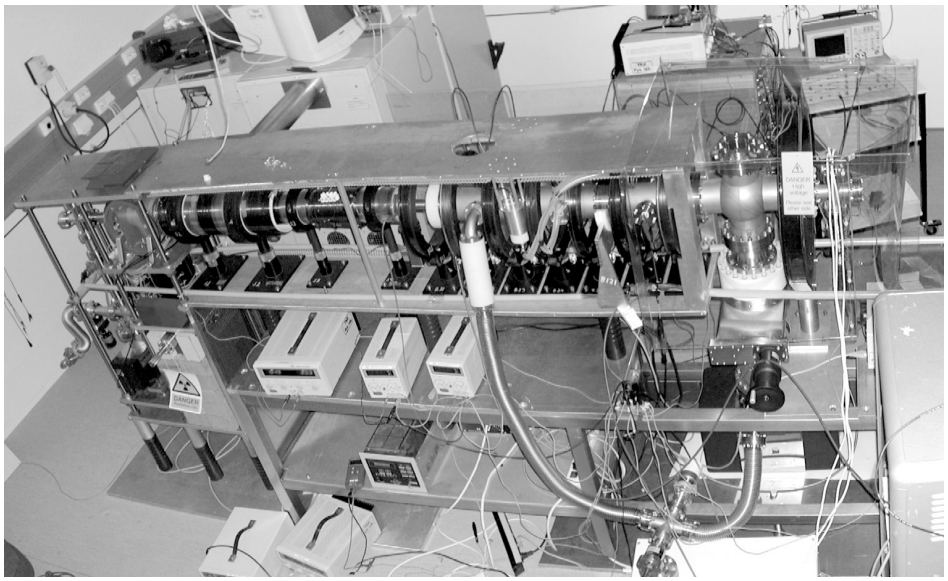

Figure 13. *Photograph of the pulsed beam without the main chamber and the Faraday cages.*

The 36 V potential is connected to the source and an extraction field is generated between the long narrow vacuum tube and the source as illustrated in Fig. 12 and Fig. 15. According to the calculations with Simion [39] and Quickfield [40] this field is linear and smooth enough at the center of the tube to exctract the slow positrons emitted from the moderator surface without increasing the momentum spread. A lead block with a circular aperture (diameter 10 mm) is placed above the source to collimate the beam and to reduce the number of fast positrons.

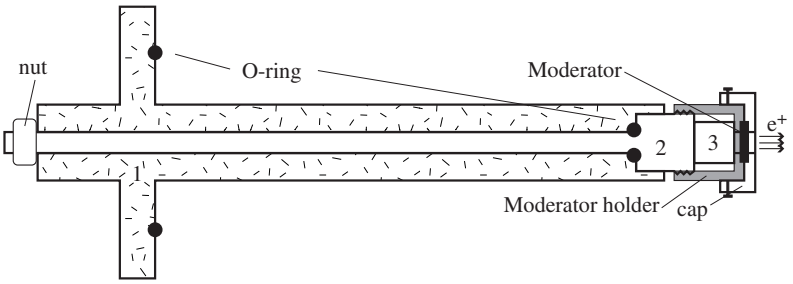

Figure 14. *Source and moderator holder. 1) insulating POM body, 2) Stainless steel center electrode, and 3) the source capsule.*

The fast positrons are separated from the slow ones by a magnetic velocity selector, which consists of two solenoids and two correction coils mounted at right angles to each other at the beam bend. Trajectories and the larmor radius of positrons change in the velocity selector and by properly choosing the field strengths, the slow positrons are guided to the horizontal part of the beam, while the fast ones annihilate at the walls of the beam. The energy of the slow, continuous positron beam is approximately 38 eV (36 V extraction potential + positron work function) when it enters the horizontal beamline [41].

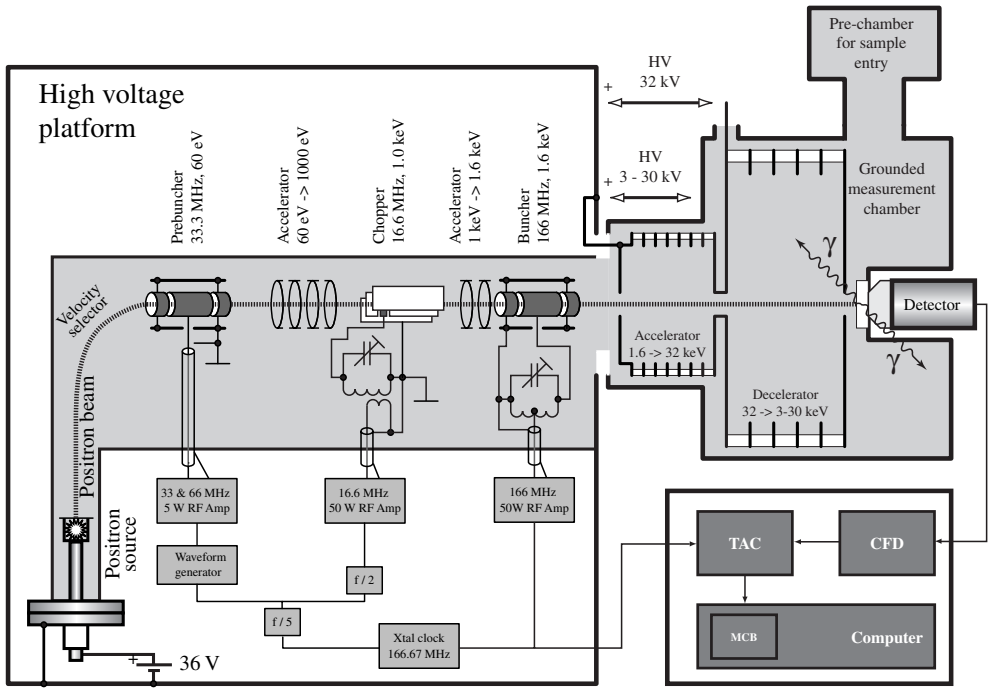

Figure 15. *A schematical illustration of the pulsed positron beam in its planned final configuration. The beam guiding solenoids and coils have been omitted for clarity. The vacuum is illustrated by shading. From Ref. [1].*

Source yield and moderator characterization The determination of the absolute value of the positron yield out of the ^{22}Na positron source has been commonly a problem [42, 43]. To overcome this, we developed two new systems to measure accurately the true number of positrons coming out of the source. In addition, these systems were used to determine the moderator efficiency so that a reliable estimate of the number of slow positrons entering the beam is available.

The first system for yield measurements is based on the measurement of the currents generated in the β+-decay process and annihilation. By using a picoammeter and properly designed measurement chamber it is possible to determine the positron yield with an accuracy better than 0.1 mCi. The measurement setup is shown in Fig. 16. The details of the measurement are described in publication [III].

The second system, a miniature slow positron beam described in detail in publication [III] and in [44], was used to verify the results of the current measurements and to determine the moderator efficiency. As a result, the positron yield of the source in the pulsed positron beam was found to be good, relative yield 33% and absolute yield at the time of measurement (March 2005) approximately 9.5 mCi. The efficiency of the single crystal W(100) moderator used in the initial tests was rather poor 2.3×10^{-5} and it was replaced with a polycrystalline W foil (thickness 3 μm) with an efficiency of 2.3×10^{-4} studied in publication [III].

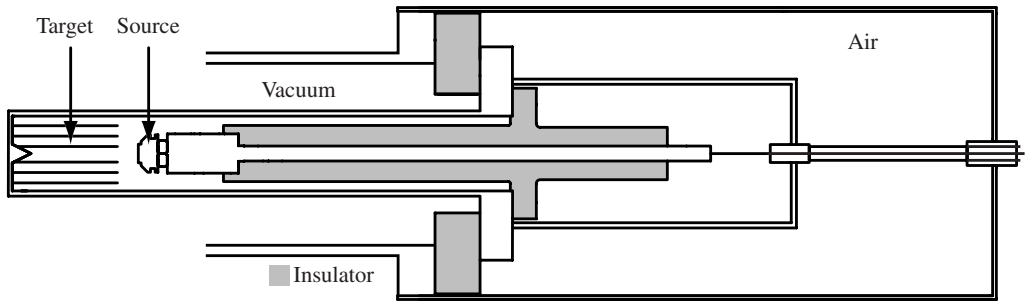

Figure 16. *Setup to determine the positron yield of the source by measuring electric currents. The source capsule is mounted on a source holder and placed inside the target-tube in a vacuum chamber. This doubly shielded structure enables the accurate measurement of the currents that are generated in the $\beta+$-decay process and annihilation.*

3.2 Beam pulsing and transport system

3.2.1 Prebuncher

The first pulsing stage is the prebuncher, which is used to increase the pulsing efficiency by increasing the number of the positrons in the time window of the main buncher. The prebuncher is a non-resonant buncher where combination of two sinusoidal voltages (33 MHz and 66 MHz) periodically accelerate and decelerate positrons in the first gap or in the second gap between the middle electrode and the end electrodes. The length of the center electrode is 40 mm corresponding to 10 ns (120° of full period) flight time when the energy of the incoming beam is approximately 38 eV. As a result the amplitudes of the f- and $2f$-components in the non-modulating gap are opposite to those in the modulating gap and no velocity modulation occurs (see Fig. 10). Base frequency of 33 MHz is chosen so that base period of the system, 30 ns is long enough for positron lifetime measurement and on the other hand is high enough to yield sufficient slew rate at the bunching gaps. The electrodes are also biased so that positrons are accelerated with constant potentials across the prebuncher as seen in the Fig. 17. The biasing minimizes the chromatical and RF-aberrations in the bunching gaps. [34, 45]

The exit electrode of the prebuncher is connected to a drift tube where the velocity-modulated positrons compress to bunches. The drift tube is followed by the first acceleration stage, preaccelerator, where the energy of the positrons is increased to 1 keV. The preaccelerator consists of five electrodes, first, third and fifth at 1000 V potential and second and fourth at the drift-tube potential. This configuration minimizes the transversal energy spread when the beam is accelerated in a magnetic field parallel to the beamline.

3.2.2 Chopper

The preaccelerator feeds positrons to the chopper, shown in Fig. 18. The chopper is made of two grounded sandwiched copper blocks with a thin double-sided printed circuit board in between them. The beam passes through the chopper via a groove machined to both copper blocks. An isolated area in the thin central copper plate acts as an electrode at the entrance end of the chopper. This electrode is part of a 16.67 Mhz resonator circuit which creates a sinusoidal electric field perpendicular to the beam. Phase of the field is adjusted so that the positron bunch from the prebuncher passes the electrode at the zero crossings (zero field) letting the bunch straight through the chopper. Between the bunches, the electric field increases the transversal momentum of the positron, which in

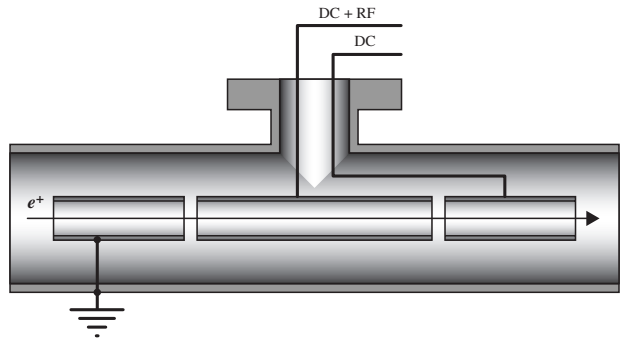

Figure 17. *The prebuncher is an unmatched double gap buncher with center electrode biased to 12 V and exit electrode biased 24 V.*

turn increases the radius of larmor precession and this causes the positrons to collide with the chopper walls. Time acceptance window of the chopper can be adjusted by varying the slew rate at the zero crossing by simply adjusting the amplitude of the chopping RF-signal. It is sufficient to use a 16.7 MHz chopping field, since the beam passes through at both zero crossings of the field amplitude resulting in a chopping action at the base frequency of the system, 33 MHz. It should be noted that this kind of 'straight-through' structure of the chopper simplifies beam alignment: when the chopper is off, the beam can directly pass through the chopping structures so that the mechanical as well as the magnetic field alignment is simple.

When low energy electrons are used to test the system (see chapter 4) care must be taken to avoid disturbance caused by the electron scattering. This is especially important in the chopper that is based on colliding the beam to the chopper walls by deflection. In this collision there is a relatively large probability for scattering and secondary electron production when the energy is in the 1 keV range [46, 47]. These electrons, which have a lower energy than those in the original beam, are detrimental to the time resolution of the beam.

Two geometrically different choppers were designed and studied experimentally [V] and the results were compared to simulations [II]. The first chopper was entitled the 'flat' chopper and the second 'sawtooth' chopper. The idea behind the latter was to

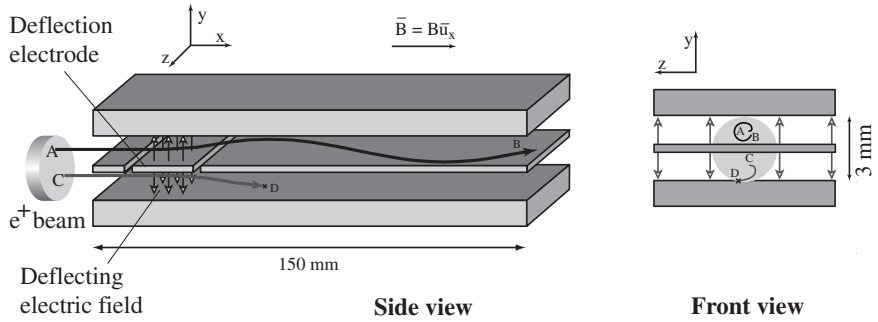

Figure 18. *The general idea of the transversal field chopping. A voltage on the electrode causes transversal velocity and associated Larmor spiralling of the positrons in the magnetic field. The positron gets through the chopper if it does not hit the electrode walls. From Ref. [1].*

design a chopper, which is opaque for the scattered and secondary electrons. Both choppers consist of a deflection plate as described earlier, followed by a long groove machined to the copper body of the chopper. In the flat chopper the groove is smooth, while in the sawtooth chopper the longitudinal cross-section of the groove resembles a sawtooth pattern (see Fig. 19). This structure consists of tilted slopes and ridges perpendicular to the beam minimizing the probability for deflected electrons to pass through the chopper. Angle of the tilted surface and height of the ridge were chosen so that mirror-like reflection does not occur in the forward direction more than once. In addition to the reflected electrons there are always secondary electrons emitted with low velocities to nearly random directions so that they can pass over the ridge and scatter again. However, probability is small for an electron to pass past all six ridges and exit the chopper. This kind of sawtooth surface has been used in large proton and positron accelerators to reduce the photoelectron emission from the accelerator chamber surfaces [48].

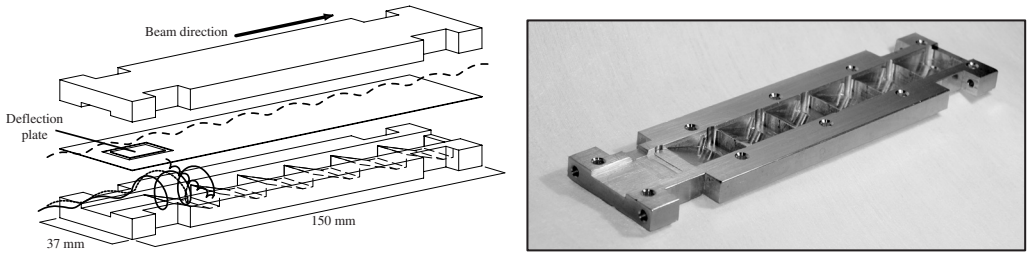

Figure 19. *The sawtooth grooves in the chopper reduce the number of scattered electrons passing through to the detector (left). Photograph of the lower half of the 'sawtooth' chopper (right).*

Electrically the chopper forms a low Q (Quality factor) resonating circuit as shown in Fig 15. The RF-signal from the power amplifier is inductively coupled to the coil of the resonating circuit. The necessary capacitance is provided by the deflection electrode and a trimmer capacitor connected in parallel with the coil. By adjusting the trimmer capacitor it is possible to tune the resonating frequency of the circuit to 16.7 MHz. The low Q-value lowers the resonator's sensitivity to temperature and helps to keep the amplitude and the frequency of the chopper stable.

3.2.3 Buncher

The principal velocity-modulating component is the main buncher, a simple single frequency sinewave double gap buncher shown in Fig. 20. In order to obtain a large time compression and a very short bunch at the target, a high slew rate is needed for the modulating voltage at the buncher gaps. This is accomplished by using both a higher frequency and a higher voltage amplitude than in the preceeding pulsing stages. The frequency, 166.67 MHz is fivefold compared to the base frequency of the system and the amplitude is approximately 200 V. To simplify the generation of this large high frequency voltage the buncher is a part of a low-Q resonator circuit.

The modulating 166.67 MHz sinusoidal voltage is generated by feeding the RF-power to the buncher through a tapped coil, which, with the center electrode and the adjustable capacitor, acts as a resonating LC-circuit (see Fig. 15). The resonator helps to lower the RF-power needed to generate the required modulating voltage. The loaded Q value of the resonator is kept below 50 so the system is quite broadband and it is subsequently insensitive to changes in temperature.

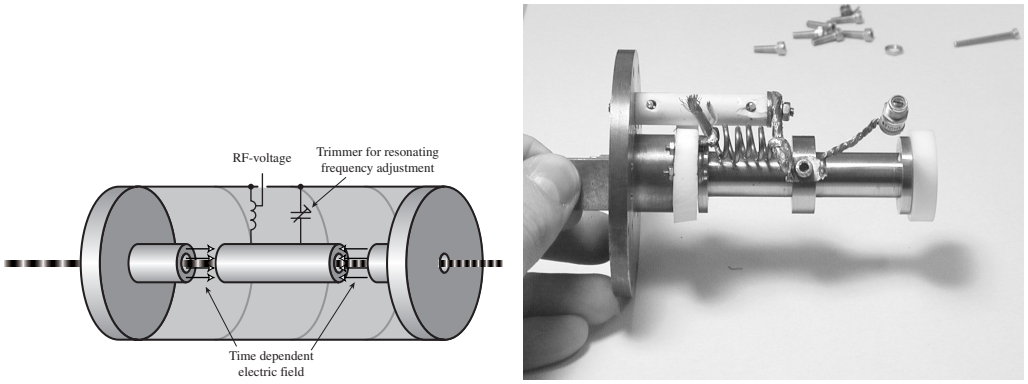

Figure 20. *The main buncher of the lifetime beam is a double gap buncher. The length of the central tube, 70 mm, is chosen so that the flight time of a 1600 eV positron through it, corresponds to a half cycle of the main bunching period. Thus the bunching field is applied twice to the positron which doubles the energy modulation.*

The RF-power required for this low Q resonator creates excess heat in the buncher coil. Therefore the other end of this coil is supported by a AlN (Shapal) rod, which, in turn is mounted on a copper flange at the end of the buncher. The copper flange is further thermally connected through a AlN insulator and copper springs to the walls of the vacuum tube. This construction increases thermal conductivity from the buncher core to the beamtube and helps to lower the temperature inside the buncher.

3.2.4 Acceleration, target chamber, beam guiding and HV considerations

The pulses from the buncher are further accelerated by a constant voltage and then slowed down to final energy in an adjustable decelerator before they hit the grounded sample. This kind of two stage accelerator-decelerator structure, shown in Fig. 21, is beneficial as it reduces the variation of the flight time through the acceleration stage with varying acceleration energies. It also helps to reduce the effects of backscattered positrons in the lifetime spectrum. These positrons are accelerated away from the sample surface and they annihilate in the walls of the large chamber at least 4 ns after the arrival of the main pulse [49].

In a pulsed positron beam it is essential that high voltages are extremely stable as the ripple in the HV leads to flight time spread in the accelerator-decelerator and this eventually deteriorates the timing spectrum. To eliminate the ripple high quality power supplies should be used and the HV structures should be designed so that no partial discharges or corona exist, which might compromise the stability of the accelerating potential. The accelerator-decelerator structure was modeled carefully with a finite element analysis software QuickField [40] to simulate many different electrode and insulator shapes and configurations. The implemented structure was tested to ensure HV stability [50].

Additionally, the publication [IV] reports the efforts done to protect the power supplies, the control electronics and the RF-system from overvoltages generated by discharges. For the DC power supplies multi-stage high voltage surge suppressors were designed and constructed. RF-power supplies are protected by commercial quarter wavelength transient protection devices. These HV related precautions are necessitated by the large size of the system. The dual Faraday cage arrangement forms a large capacitor ($C \approx 1$ nF) and when the system is floating in high voltage the amount of the stored energy is of the order of 1 J. If this energy is released in an uncontrolled fashion i.e. by

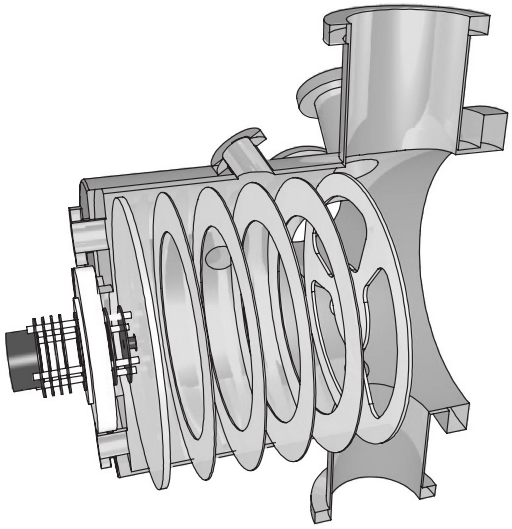

Figure 21. *The accelerator-decelerator structure minimizes the flight time spread with different energies and helps to get rid of backscattered positrons.*

a HV breakdown, large surge currents are generated, which in turn can generate serious overvoltages in the control and the power supply system.

The beam is guided magnetically from the source to the target with solenoids and coils as shown in Fig. 12. The magnetic field is 60 Gauss in the floating part of the beam and 110 Gauss in the target chamber. The larger field in the target chamber is necessary to guide the backscattered positrons away from the sample [1, 49]. In the vertical part of the beam and in the first half of the horizontal beamline the beam is guided by solenoids with some additional coils to steer the beam and to compensate the magnetic field of the ion pump in the source area. The latter half of the floating horizontal beamline as well as the target chamber are surrounded by Helmholz coils due to the space restrictions. Both the solenoids and the Helmholz coils can be adjusted independently. The earth's magnetic field is compensated by two large horizontal coils surrounding the whole beam (not shown in Fig. 12). All the larger coils are powered by switching power supplies from Delta Elektronika, Netherlands. Smaller coils are supplied from linear laboratory power sources.

3.3 RF-electronics, control system and signal detection

3.3.1 RF-electronics

The pulse generation is controlled by electronics, which also provides the necessary timing signal corresponding to the time when positron enters the sample. The simplified diagram of the pulsed positron beam RF- and timing signals is shown in Fig. 22.

The main oscillator is a 166.667 MHz oscillator from Vectron Inc. The sinewave clock signal is split into two branches by a power splitter, one branch is connected to the buncher electronics and the other is sent to a frequency divider. This frequency divider is made from 1:5 prescaler from National Semiconductors. The resulting frequency of 33.33 MHz is then again split to 3 branches in a 3-way power splitter. One branch is connected to the prebuncher, the other to the chopper and the third to a fiber optical link.

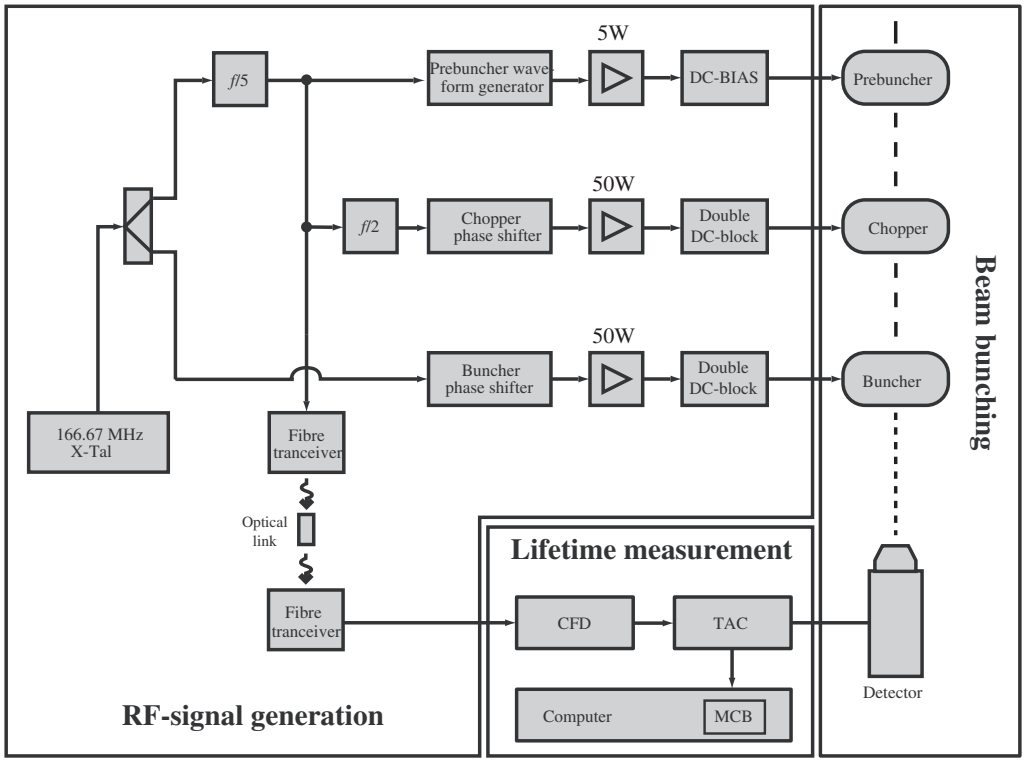

Figure 22. *The RF-system and detector system of the pulsed positron lifetime beam.*

The prebuncher branch is used as an input signal for synthesizer where a prebunching waveform is generated. This is done by creating a second harmonic at 66.66 MHz and summing it with the base frequency 33.33 MHz in a power combiner. Amplitude of both signals can be adjusted by current controlled bi-phase variable attenuators. The generated waveform is then fed to a 5 W power amplifier (MiniCircuits ZHL-5W). The amplified signal is connected to the prebuncher via a DC-block, used for biasing the prebuncher middle electrode to 12 V DC.

The second 33.33 MHz branch to the chopper is connected to a 1:2 frequency division circuitry employing a ripple carry divider and a low pass filter to create 16.67 MHz sinewave at its output. The phase and amplitude of this signal is controlled by a simple phase shifter [45, 51]. The sinewave is amplified by a 50 W power amplifier (MiniCircuits LZY-1) before the double DC-block (described below) and impedance-matched connection to the chopper. The 166.67 MHz signal to the buncher is phase adjusted, amplified and connected to the beamline similarly.

The third branch of the 33.33 MHz signal is used for timing of the beam via a fiber-optic link. This link, which consists of a transmitter and a receiver from Agilent technologies is capable of transmitting signals up to 155 MBd/s with plastic multimode fiber. At the ground potential the ECL-level timing signal is DC-blocked and connected to the time to amplitude converter (TAC) to provide the stop signal. The start signal from the detector (see below) is connected to the TAC via a constant fraction discriminator. The timing spectrum from the TAC is collected with a multichannel buffer attached to a computer.

The stability of different RF-components were studied and results were satisfactory: the thermal stability for all components was found to be below 10 ps/°C for the phase and less than 0.04 dB/°C for the amplitude. Another possible source of instabilities for these components is the supply voltage, which in turn should be constant with an accuracy of 1 % or better. [51]

As both the chopper and the buncher are floating at a high potential, 1 kV and 1.6 kV respectively, both the inner and the outer connector of the coaxial feedline has to be DC-blocked. This is done by using a 'double' DC-block (both signal and ground connections are isolated) made of high-voltage, high-Q ceramic capacitors in a coaxial arrangement. These DC-blocks introduce a serial capacitance that can be utilized when the resonator is matched to the amplifier. This impedance matching for both the chopper and the buncher is done by placing double stub tuning elements made of semi-rigid coax between the DC-blocks and the pulsing components in the beamline. [52]

3.3.2 Control electronics

The floating source and pulsing system is challenging for the control and the monitoring of the beam. To solve these issues it was decided to use a remote control via fiber optical ethernet connection using robust IO-modules at the high voltage. The selected FieldPoint IO-system from National Instruments provides a large variety of different analog and digital input and output modules and it is easily extensible. The modules are simple to program and they can be controlled via TCP/IP network from LabVIEW graphical programming environment.

3.3.3 The Detector

Timing signal for the positron annihilation is measured by a BaF_2 scintillation detector placed behind the sample. Shape of the BaF_2 crystal is a truncated pyramid with cleaved wedges with an octagonal profile at the base and a square profile at the top. The scintillator is attached to a Philips XP2020Q photomultiplier tube (PMT) with Rhodosil 47 V optical glue, which is transparent at UV wavelengths as well as for visible light. The PMT is fitted to a PMT base inside the detector well. The timing signal is taken from the anode.

As the detector is inside the magnetic field generated by Helmholz coils, it is placed into a magnetically shielded detector well. The magnetic shielding is realized in three stages. The first shielding stage is the end cap of the detector well which is made of μ-metal. The second stage is a thick cylinder with a narrowing cone with an opening for the scintillator at the other end. This cylinder is made of AD-MU 40 material (from Ad-Vance Magnetics, Inc.), which has lower permeability than μ-metal but does not saturate as easily as μ-metal. The third and the innermost stage is made of μ-metal and it reduces the magnetic field to 0.1 Gauss level. In order to minimize the field at the photocathode, where the PMT is the most sensitive to the external field, an active compensation coil of 20 ampereturns can be placed at the scintillator end of the well, between the second and the third stages of the shielding. [53]

4 Results of test measurements

In this chapter the results of the test measurements with the pulsed positron lifetime beam at HUT are presented. This chapter refers to the publications [II, V] in this thesis.

4.1 Electron tests

4.1.1 Background and measurement setup

Timing properties of the beam can be determined with positrons and a suitable target e.g. stainless steel using a scintillator and a photomultiplier tube (PMT) as a detector. When the system is tested it is advantageous if the measurement times are short and and the resolution good. This can be accomplished if the positron source is replaced with an electron gun and a fast microchannel plate (MCP) is used as a detector.

Testing of the system requires that the timing spectra can be obtained fast and accurately. With conventional isotope sources and moderators and a BaF_2 scintillator detectors the count rate is limited to hundreds of counts per second resulting in relatively long measurement times. In our case it is also difficult to provide the necessary magnetic shielding for the photomultiplier tube of the detector in the test configuration of the beam.

To overcome these limitations we developed a new method for testing of the timing properties of a pulsed positron beam. We used a small, low-temperature electron source to obtain a narrow electron beam with high brightness. This enables to obtain easily high, controllable count rates. As a detector we used a microchannel plate, which is insensitive to magnetic fields. Other additional advantages of this setup are: (i) the energy distribution of the beam is narrower, (ii) the beam diameter is much smaller compared to that generated from a positron source and (iii) the time resolution of the MCP detector is better than the resolution of a scintillator detector.

The electron source was a self-made electron gun where a BaO-disc (Kimball Physics ES-015 BaO cathode) was used as the electron emitter. An adjustable slit was placed 250 mm away from the electron gun to reduce the electron current to sub fA-level during timing tests. The electron gun was also used for beam alignment, where a phosphor screen and a picoammeter were used as beam monitors.

Timing detector, a microchannel plate (Hamamatsu F4655-12), was mounted next to the buncher and it was floating at 2.6 kV. The accelerator-decelerator structure was not employed. It was observed that the MCP was very sensitive to the residual gas ions and electrons created in the ion pumps. Therefore, the system was pumped only with turbopumps during the tests. The start signal from the MCP to the timing electronics was connected through a insulated BNC-feedthrough and 'double' DC-block (described earlier). The stop-signal was obtained from the pulsing electronics via a fiber optic link.

4.1.2 Results

The flat chopper and the chopping power The electron scattering effects in the flat chopper are illustrated by the timing spectra shown in Fig. 23. In this figure the timing spectra for a beam that was only chopped, are shown. With a low amplitude of the field in the chopper (dashed curve) the peak is broad and the background is high. When the field amplitude is increased the peak gets narrower and the background becomes asymmetric (solid curve) showing a larger number of electrons arriving earlier (right hand side).

This asymmetry can be understood if the spectrum is thought to be composed of two spectra: the chopped spectrum and the background spectrum due to scattered electrons.

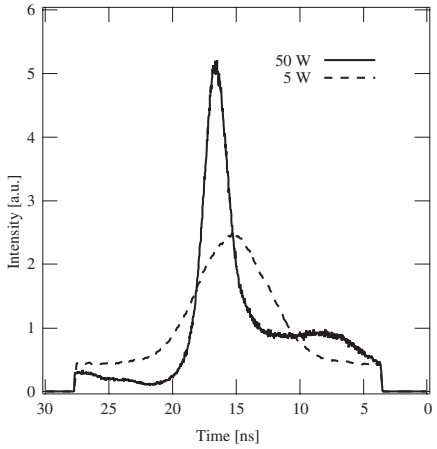

Figure 23. *Increasing the chopping power from 5 W to 50 W narrows the pulse but changes the pulse shape due to scattering and secondary electron effects.*

The electrons in the chopped spectrum have passed through the chopper with unmodified energy when the chopping field is negligible in the chopping window and no scattering occurs. The background spectrum is from those electrons that arrive outside chopping window and have been deflected and subsequently scattered. In the inelastic scattering the electrons lose energy and the flight time to the target increases. This causes the background spectrum to shift to later times i.e. to left and the 'hole' in the background spectrum (due to chopped spectra) appears on the left hand side of the main peak. This explains the 'shoulder' on the right hand side of the main peak, which is due to electrons scattered during the previous cycle of the deflecting field. This effect is not visible in the low amplitude spectrum since the chopping window is large and the chopping amplitude too low so that some electrons can pass through the chopper all the time and the number of inelastically scattered electrons is low. Thus, the background due to scattering is constant. From these results, it is evident that the flat chopper is not suitable for lifetime beam.

The sawtooth chopper The results from the measurements with the sawtooth chopper and using all pulsing components are shown in Fig. 24. The amplitudes and phases of different pulsing components were adjusted to yield as narrow final bunches as possible. The topmost curve shows how the prebuncher compresses electrons into the chopping time window increasing the efficiency of the beam (curve (a)). The full width at half maximum (FWHM) is 3.1 ns and the asymmetry of the peak can be explained by the phase difference between f and $2f$ components in the prebuncher waveform. The spectrum shown by the curve (b) is collected when only the chopper is active. It shows that the chopper works: the FWHM is 2.3 ns, the background is flat and low and the peak-to-background ratio is approximately 100:1. When the prebuncher and the chopper are operating simultaneously, the peak-to-background ratio improves to 300:1 and FWHM of the peak is 1.8 ns, as seen from the curve (c).

The spectrum recorded with only the main buncher on is shown by curve (d) in Fig. 24. The periodic structure of five similar peaks is due to the 6 ns main bunching period in a 30 ns base time window (166.67 MHz bunching rate vs. 33.33 MHz base frequency). The width of an individual peak is good, 160 ps, but the background is high (P/B ratio of 30:1).

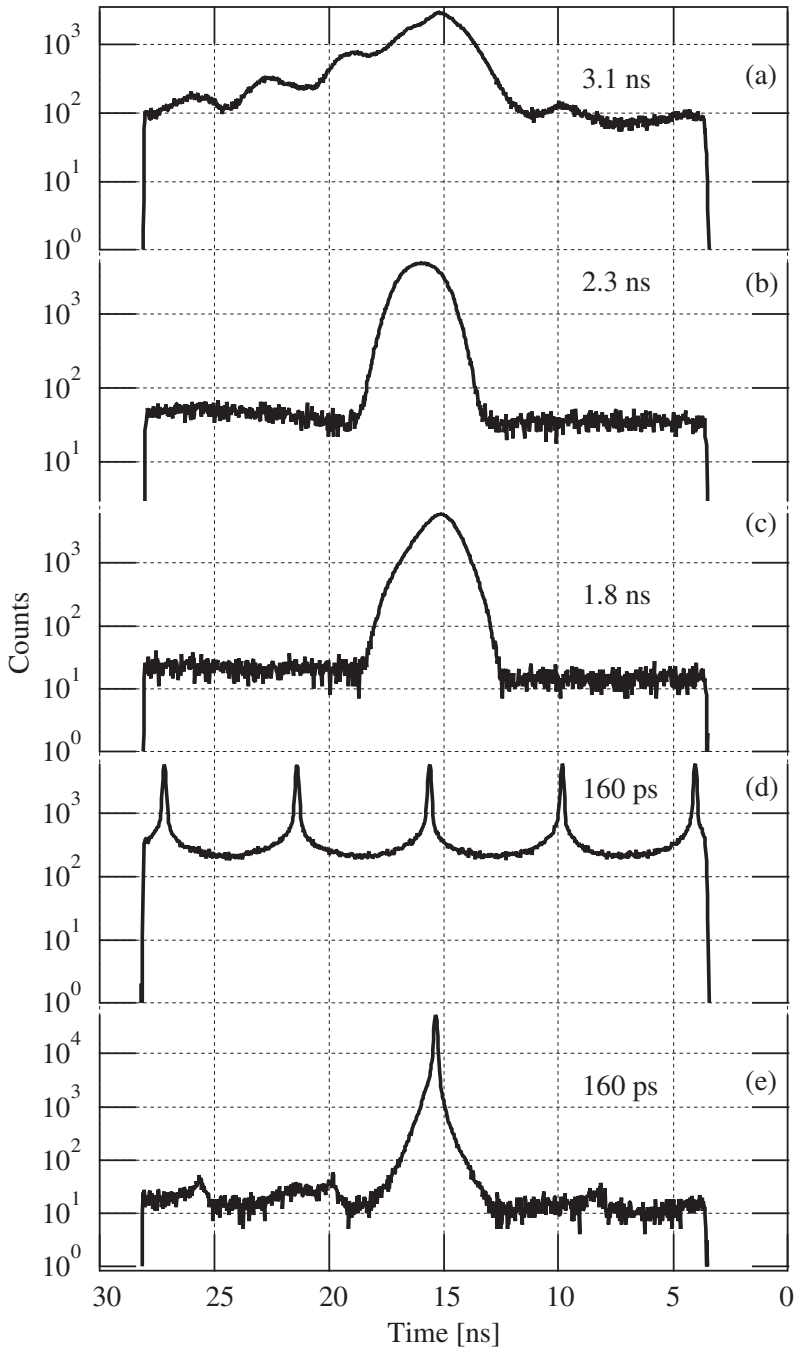

Figure 24. *The spectra measured from the bunchers and the chopper and their combinations show that a time resolution of 160 ps, is obtainable with the sawtooth chopper. (a) prebuncher, (b) chopper, (c) prebuncher and chopper, (d) buncher and (e) all together. The FWHM for each component and their combinations is given in the figure.*

When all pulsing stages are operating, the spectrum of Fig. 24 curve (e) is obtained. The signal phases of different pulsing components have been adjusted so that the middlemost bunching peak matches the prebuncher and chopper time windows. The FWHM of the final peak is 160 ps. The peak-to-background ratio is good, better than 5000:1. The background is not completely flat, due to the five main bunching periods during one base operating cycle. This uneven background should not be a problem for data analysis, since its shape is not dependent on the acceleration energy and thus it can be subtracted from the data. If the peak positions in the spectra in Fig. 24 are compared, a small peak shift is observed when the prebuncher is on. This is due to a small additional energy introduced by the RF acceleration in the prebuncher because of non-optimal initial energy of the beam [54].

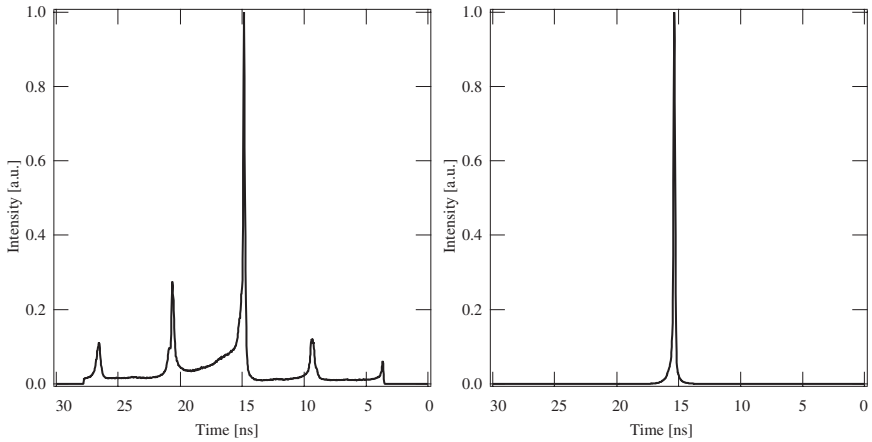

Figure 25. *The time spectrum measured with the flat (left) and the sawtooth (right) chopper when all pulsing components are on. The FWHM 160 ps is good in both cases, but the background and peak-to-background ratio is relatively poor for flat chopper.*

Comparison between the sawtooth and the flat chopper The measured timing spectra using a flat chopper and the sawtooth chopper are compared in Fig. 25 (right hand side is same as curve (e) Fig. 24, but now with linear scale). The superiority of the sawtooth chopper over the flat one is evident: the flat chopper spectrum shows side peaks, the peak-to-background ratio 1:10 is low and there is a significant nonlinear background. None of these problems are present in the spectra obtained with the sawtooth chopper.

Results from simulations The publications [II] and [V] presents the computer simulations that were done to compare the properties of the two chopper designs. The main challenge of the simulation is the treatment of the scattering in a proper way. Theoretical and experimental data of scattering probabilities and secondary electron yields were found from the literature [46,47]. Also, detailed studies using a model presented in publication [II] were done. As a result it was found that a simple model where 33 % of electrons colliding with the wall scatter elastically and 67 % inelastically is sufficient to describe the scattering. The elastically scattered electrons were assumed to reflect from the surface, while the inelastic ones lose on average 40 % of their energy in the scattering. The direction of the inelastic scattering is randomized but weighted in the calculation so that it points to the direction of forward scattering.

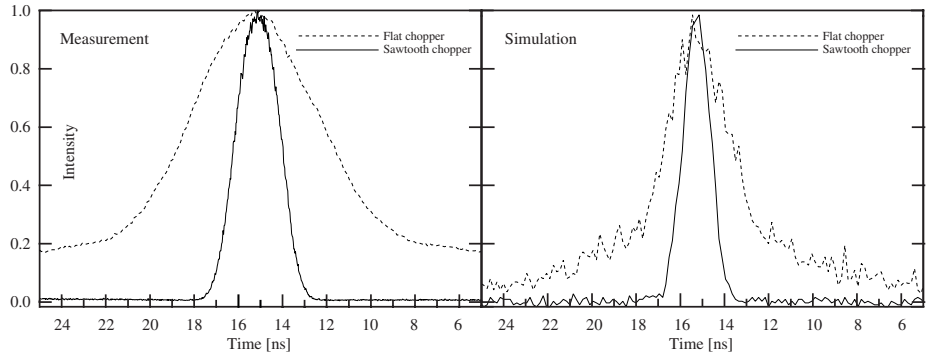

Figure 26. *Both the measured and the simulated spectra for the flat and the sawtooth chopper show that the introduction of the grooves improves time distribution significantly.*

Measured and simulated spectra for the two chopper designs are compared in Fig.26 (the measured and calculated time distributions here are for a beam that is only chopped with a low power RF-amplifier). It is clearly seen from the measured data (left in Fig.26) that the sawtooth chopper gives significantly better results compared to the flat chopper: the background is negligible and the peak is narrow. This result is verified by simulations seen in the right hand side of Fig.26, which replicate the measured spectra relatively well. These results suggest that the electron scattering and secondary electron generation plays an important role in the shape and the width of the final timing spectra.

4.1.3 Conclusions from electron tests

The electron tests show clearly that it is possible to test pulsing properties of a pulsed positron lifetime beam with electrons. For successful tests the beam chopper should be designed properly, in this case a sawtooth design was used to prevent electron scattering through the chopper. This design improves the system performance also with positrons by reducing positron scattering. The results of simulations show that it is possible to simulate the electron scattering in the beam realistically and estimate its effects to the final time distribution.

The electron gun and a MCP proved to be an efficient way to study timing properties of a pulsed beam and to obtain accurate results rapidly. Tests showed that our system is working in the expected way with electrons and we can obtain a FWHM of 160 ps for the peak and a peak-to-background ratio better than 5000:1 in its test configuration.

4.2 Positron tests

When the electron source was replaced with a positron source it was decided to use the microchannel plate as a detector in order to simplify the comparisons between the electron timing spectra and the positron timing spectra.

The spectra resulting from these measurements are shown in Fig. 27 (the results of the electron tests are replicated for clarity). The labels associated to the different spectra denote the pulsing components that were active while the spectra were collected.

The prebunched positron beam peak is very flat and exhibits no features present at the corresponding electron spectrum. Several reasons for this poor preliminary performance were found: (i) The positron moderator was slightly tilted, resulting in momentum spread and misalignment of the beam, (ii) the extraction voltage had 50 Hz AC line interference, and (iii) the bunching voltage at the prebuncher was only a tenth of the maximum. In

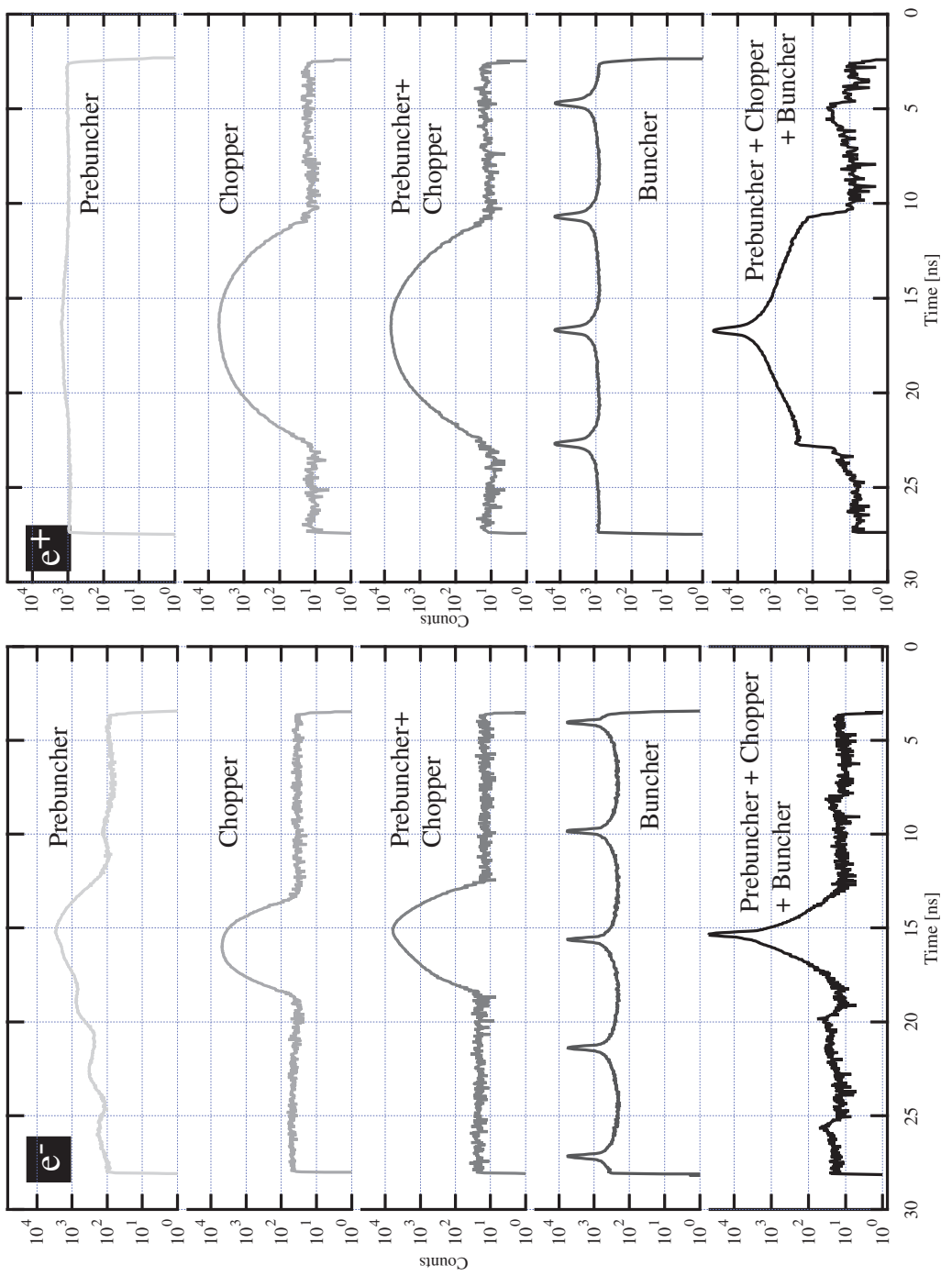

Figure 27. *Timing spectra for electrons and positrons measured from the separate pulsing components and their combination. The FWHM for completely pulsed beam is 165 ps for electrons and 270 ps for positrons.*

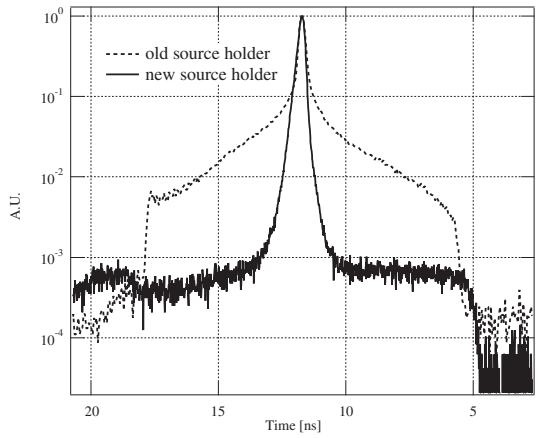

Figure 28. *The timing spectrum of the pulsed positron beam measured with a MCP. The spectrum acquired using the new source holder is clearly better than the one measured with the old holder. The FWHM is 270 ps and P/B-ratio ratio is better than 1:4000.*

spite of these technical difficulties, the prebunching action is observable in Fig. 28.

The spectrum obtained by chopping the beam is surprising: the FWHM is more than double compared to the similar electron spectrum but the peak-to-background ratio is significantly better, 500:1. These features can be explained as follows: The main reason for the increased peak width is the initially significantly larger radius of the positron beam compared with the electron beam. This increased radius increases the time needed in the chopping to cut out the beam completely, since to deflect the positrons flying far away from the beam axis a higher deflection field and a longer time is needed.

Another contribution to the broad peak is the initial increased energy spread of the positrons due to tilted moderator. Effect of this is less significant. The improved peak-to-background ratio proves the chopper to be very efficient for the positrons – the sawtooth structures prevent the positron scattering while for electrons some very low energy ones might still get through.

The combined spectrum of the prebuncher and chopper is practically identical to the chopper spectrum due to practically inactive prebuncher. The spectrum obtained with the buncher only is quite similar for both positrons and electrons. However, the FWHM is somewhat larger, 250 ps, and the P/B-ratio 1:20 for positrons.

Finally, the last spectrum where all the pulsing components are working shows a spectrum that has a FWHM of 270 ps. However, in the logarithmic scale the shape of the peak and the background are not optimal even though the P/B ratio is excellent 4000:1. This spectrum is compared to a spectrum measured with the new source holder in Fig. 28. The base of the peak is broadened, otherwise the spectra have acceptable shapes. The result is very promising and proves that the implementation of the pulsed positron lifetime beam was successful. Minor modifications like installing the improved source-moderator holder, improving the stability of the extraction voltages and collimating the beam can be expected to improve the results close to those obtained with electrons.

It can also be expected that the positron lifetime spectrum has similar features as the timing spectrum measured with a MCP. However, it should be noted that when the beam timing properties are studied, the lifetime measurement does not provide any improvement over a timing measurement conducted with an MCP, but vice versa, the lifetime measurement has poorer resolution and lower count rate.

5 Positron lifetime beam measurements on InN layers

Since the measurement chamber, sample holder and the detector system were under construction and testing, the positron lifetime measurements were not possible with our system. In order to gain experience and knowledge the author carried out pulsed positron beam measurements at Universität der Bundeswehr, which has the only working lifetime beam system in the Europe at the moment. This chapter reviews the results of these measurements and refers to publications [VI, VII].

5.1 Background and experimental

The group III-nitride semiconductors GaN and AlN are interesting materials for applications in short-wavelength optoelectronic devices. Recent results suggest that indium nitride may have a bandgap of only 0.8 eV [55, 56]. Hence, InN could extend the wavelength range of III-N materials into the infrared region. The high theoretical electron mobility and the peak drift velocity also make InN a promising material for high speed electronics [57, 58]. The fabrication of device-quality InN has, however, been very difficult. One of the problems is related to the doping of InN. Due to donor states of unknown origin, the grown InN layers are highly n-type, and p-type doping has not been achieved. According to calculations, the impurities O_N and Si_{In} have the lowest formation energies of the donor-type defects [59], but also interstitial hydrogen is suggested to cause the n-type conductivity [60, 61].

Additionally, at the moment no bulk InN material exists and only epitaxially grown layers are available. However, a problem with these layers is the lack of a suitable substrate material. The large lattice mismatch with the often-used Al_2O_3 substrate leads to a high density of extended defects. Experimentally, the dominant point defects have not been identified and their concentrations are not known. Therefore, we applied positron annihilation spectroscopy to study native vacancies in InN layers. The layers can be routinely studied with Doppler broadening spectroscopy utilizing slow positron beams. On the other hand, positron lifetime spectra are required to achieve a full understanding of the results from positron annihilation spectroscopy, since only the lifetime experiment is able to distinguish unambiguously between positron annihilations in the lattice and those at vacancy defects. In the following the results from the measurements with both slow positron spectroscopies are discussed.

5.2 Results

Results from the Doppler broadening experiments Figure 29 shows the S parameter measured as a function of the positron beam energy (depth scan). At low positron incident energies ($E < 3$ keV) a fraction of the positrons is able to diffuse to the sample surface before annihilation. The high S parameter observed at low energies results from annihilations at the sample surface. In two of the samples (#1 and #4), the thin AlN cap on top of the InN layer is also visible in the curves. When the positron energy is increased, fewer positrons can reach the surface and the S parameter corresponds to annihilations inside the InN layer. The S parameter characteristic of the InN layer can be seen as a constant plateau in the curves. At higher implantation energies the S parameter starts to decrease as positrons are able to reach the Al_2O_3 substrate below the InN. This turning point in the curves corresponds roughly to the layer thickness, except in sample #3 which was thinner than expected from its nominal thickness.

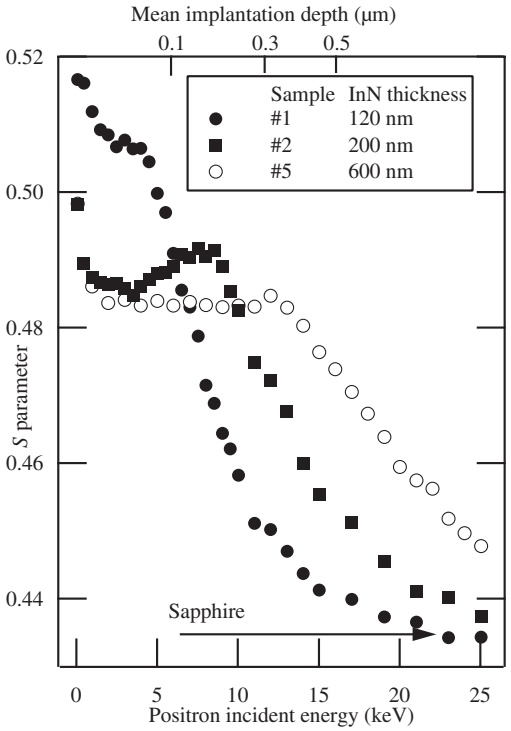

Figure 29. *The S parameter vs. positron beam energy for three different layers. The level associated with the sapphire substrate is shown with an arrow.*

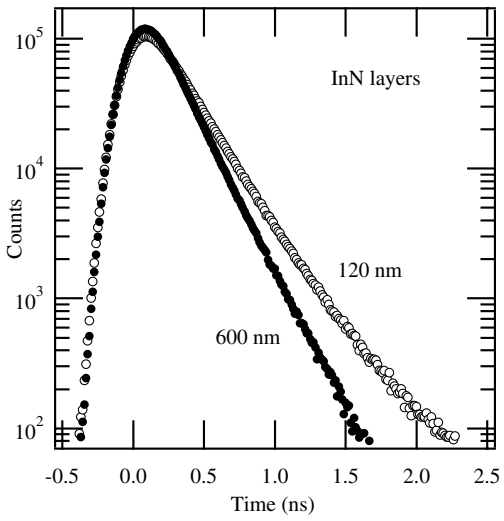

Figure 30. *Positron lifetime spectra from samples with 600 nm (black circles) and 120 nm layer (open circles) thicknesses. The spectra were measured with positron incident energies of 3 keV (120 nm layer) and 8 keV (600 nm layer).*

The lowest S parameter, $S \approx 0.483$ is found in the thickest (600-nm and 800-nm) layers (only #5 shown in Fig. 29). In the thinner layers the S parameter is clearly higher. The increased S parameter indicates that positrons get trapped at vacancy type defects. In two of the samples (#2 and #3), the S parameter increases towards the interface, suggesting that the vacancy concentrations are higher in the interface region.

Positron lifetime results The positron lifetime experiments, performed with the pulsed beam facility on four samples (#1, #3, #4, and #5) show very similar results compared to the Doppler measurements. The differences between samples are demonstrated in the lifetime spectra of Fig. 30. The 120 nm InN layer had clearly longer positron lifetime components than the 600 nm thick sample, indicating vacancies in the thinner layer. The average positron lifetime τ_{ave} was 190 ps in the thickest layer (#5). In the thinnest layer, where the S parameter was also the highest, the average positron lifetime increased up to 260 ps.

The average positron lifetime τ_{ave} is plotted against implantation energy in Fig. 31. The lifetime distribution shows features similar to the S parameter in Fig. 29. The average lifetime in the layer decreases with increasing layer thickness. The significant increase in the average lifetime near the sample surface (low energies) is associated with positron diffusion to the surface where the positrons get trapped by surface states with

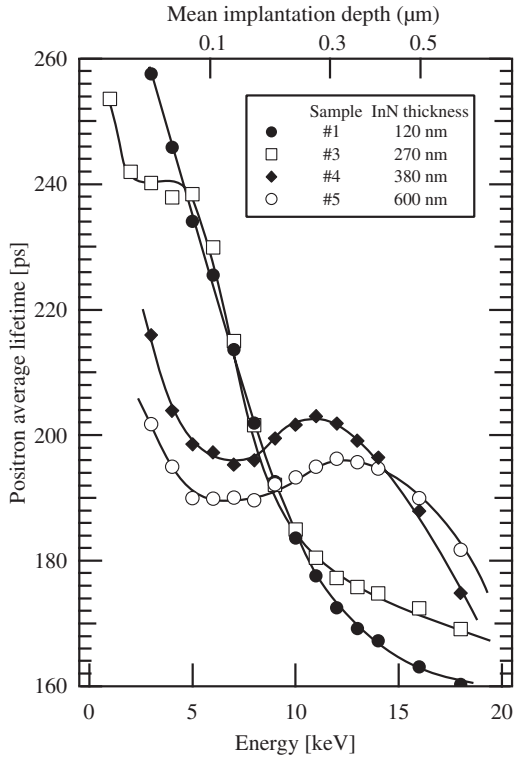

Figure 31. *The average positron lifetime τ_{ave} vs. positron beam energy (depth scan) for four different layers. The corresponding mean implantation depth of positrons is indicated on the top axis. The lines are only a guide to the eye.*

a long positron lifetime. The higher vacancy concentrations in the interface region can also be seen in the lifetime data of samples #4 and #5 as a slight increase in the average positron lifetime.

5.3 Identification of In Vacancy

Number of vacancy defect species by linearity analysis The linearity between the annihilation parameters S, W and τ_{ave} can be utilized to investigate the number of different positron states in the samples [2]. The (S, W) plots, with positron energy as a running parameter, are shown in Fig. 32. When the positron energy is increased, the (S, W) points move from their surface values towards those specific for the InN layer, and finally towards the (S, W) point of the sapphire substrate. Data points form a straight line between the sapphire and the InN layer, indicating no strong contribution from the interfaces or from the buffer layer. The (S, W) parameters specific to each InN layer could thus be unambiguously determined.

Fig. 33 shows the layer-specific S and W parameters in each sample. The (S, W) points form a line, indicating that positrons annihilate in two states: as free positrons, characterized by the annihilation parameters for defect-free InN (S_{b}, W_{b}), and as positrons trapped at a particular vacancy (S_{V}, W_{V}). Similarly, the functional relationship between the positron average lifetime and the S parameter is linear (Fig. 33), indicating again that the vacancy in each of the layers is the same [2].

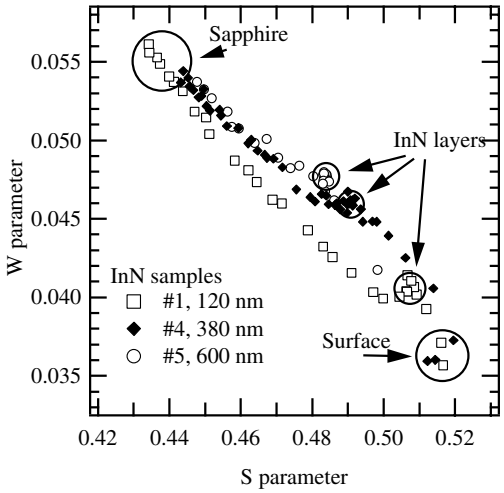

Figure 32. *W vs. S plot (positron beam energy as a running parameter) in three InN samples. The layer-specific parameters are clearly distinguished from the surface and sapphire substrate. Data points form a linear line between the sapphire and the InN layer, demonstrating no strong positron trapping effect at the interface.*

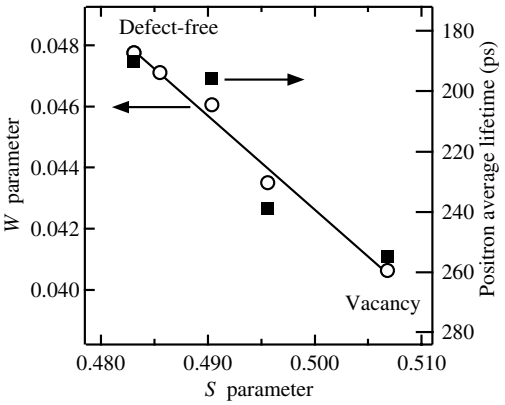

Figure 33. *The S and W parameters, and the average positron lifetime in the InN layers. Positron beam energy was kept in the range $E = 3 - 7$ keV so that the layer-specific annihilation parameters were recorded. Linearity between S and W, and between S and τ_{ave} indicates that the same vacancy is present in all layers.*

Identification by chemical neighborhood and open volume The identification of a vacancy defect can be based on both electron density (positron lifetime) and momentum density (Doppler spectroscopy) data. In Fig. 34 the high momentum part of the 511 keV annihilation line is shown for samples #1 and #6, measured with positron energies corresponding to the middle of the InN layer. The Doppler broadening spectra were recorded with a two-detector (Ge-BGO) coincidence set-up to reduce the background level [2]. In Fig. 34 the theoretical momentum distributions, which were calculated by using atomic core electron wave functions [62,63], are shown also for three different cases: the annihilations of free positrons in the defect-free InN lattice, and the annihilation of positrons trapped at In and N vacancies.

Above $15 \times 10^{-3}\, m_0 c$ the momentum distribution mainly consists of the annihilations with the atomic core electrons and therefore provides information on the atoms around the annihilation site. In the case of free-positron annihilation in defect-free InN the strongest contribution to the high-momentum area comes from annihilations with the 4d-electrons of indium. For the N vacancy the calculated wavefunction of positrons overlaps strongly with the neighboring In atoms, resulting in a momentum distribution very similar to that for free-positron annihilation. For the In vacancy, the strongest contribution also comes from the 4d-electrons of indium, but as the In atoms are now the second nearest neighbors, the intensity of the high momentum range is clearly smaller. The intensity reduction between the measured momentum distributions in the samples #6 (low vacancy concentration) and #1 (high vacancy concentration) indicates that the observed vacancies are In vacancies.

Further evidence is provided by the changes in the shape of the momentum distributions. As can be seen in Fig. 34, the slopes of the momentum distributions are slightly different for the vacancy (sample #1, 120 nm) and lattice (sample #6, 800 nm). This

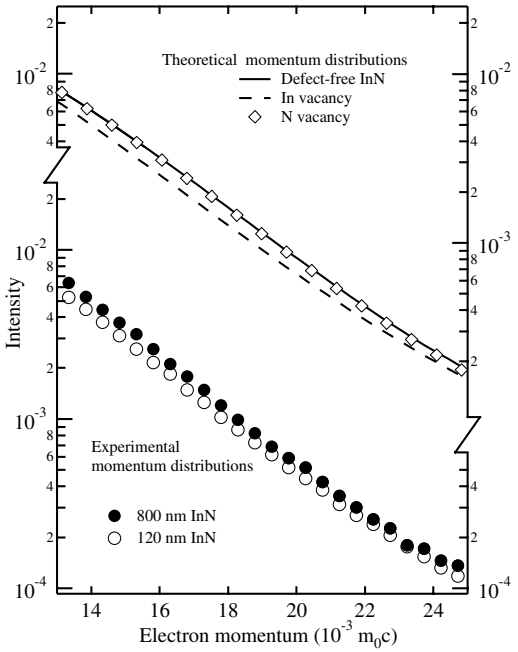

Figure 34. *The core electron momentum distributions in the InN layers. The lower panel presents the experimental results for samples #1 and #6, measured at beam energies of 2.5 and 7 keV, respectively. The upper panel shows the results of theoretical calculations for the InN lattice and for vacancies in both sublattices.*

small effect is due to N 2s and N 1s electrons, which have high momenta and enhance the intensity at (20-25) $\times 10^{-3}$ $m_0 c$ in the curve obtained for the vacancy (sample #1, 120 nm). The vacancy is thus surrounded by N atoms, i.e. it is the In vacancy.

The identification of the In vacancy is supported also by the positron lifetime experiments. The positron lifetime in a defect-free InN lattice was calculated using the atomic superposition method [63, 64] as 184 ps, and the lifetimes of positrons trapped at N and In vacancies were calculated as 186 ps and 260 ps, respectively. These are close to the experimental average positron lifetimes of 190±2 ps and 260±2 ps in samples #1 and #5, respectively (Fig. 33). Although the decomposition of the measured lifetime spectra into free-positron and vacancy-related components is difficult, the observed difference of about 70 ps between the average positron lifetimes in the thin and thick samples (Fig. 33) can result only from positron trapping at In vacancies.

5.4 Conclusions from InN measurements

In summary, vacancies in MBE-grown InN layers with positron annihilation spectroscopy, using both positron lifetime and Doppler broadening measurements were observed. Concentration of the vacancies decreases with increasing layer thickness. The defects are identified as In vacancies. The increase in $[V_{\mathrm{In}}]$ from below 10^{16} cm^{-3} to above 10^{18} cm^{-3} for films of increasing thickness correlates with the increase of the free electron density. This behavior is typical for a compensating center. The concentration of In vacancies also anticorrelates with the electron Hall mobility, suggesting that the $[V_{\mathrm{In}}]$ may significantly limit electron mobility in the thinner layers.

6 Summary

Positron annihilation spectroscopy can be used to identify vacancy type defects in semiconductor samples. Identification of both vacancies and their surrounding atoms can be conventionally done only for bulk samples that can be measured with both lifetime and Doppler broadening spectroscopy. The pulsed positron beam facility described in this work provides a method to measure positron lifetime in thin semiconductor layers. This enables direct identification of the open volume of the defect in layers, more straightforward determination of vacancy concentrations, and improved sensitivity compared with Doppler measurements.

This work begins with a brief introduction in chapter 1. In chapter 2 the theoretical concepts behind the beam pulsing techniques are introduced and mathematical formulas and illustrations are derived to provide background for the understanding of the beam pulsing.

Chapter 3 presents the design and the technical implementation of the pulsed positron beam facility and introduces some parts and concepts in more detail. The system constructed in this work is composed of a source area, floating at high voltage, and a target at the ground potential. The source area contains all the pulsing components as well as all the electronics necessary to control them. The beam is generated from a continuous monoenergetic low-energy positron beam from a moderated isotope source by a three-stage pulsing. First, a prebuncher is used to improve the beam efficiency. Second, a chopper removes the background from the prebunched beam and finally the main buncher provides the large energy modulation needed for the creation of very short positron pulses. Acceleration of the bunched beam happens in the decelerator-accelerator structure between the high voltage area and the grounded target.

Results of the test measurements are summarized in chapter 4. The electron tests show that the beam facility works as expected, the width of the pulse at the target is 160 ps and the peak-to-background ratio is better than 1:5000. The positron tests show a bit larger pulse width, 270 ps and the peak-to-background ratio is approximately 1:4000. The background with positrons is not completely smooth. However, already these preliminary results show that the implementation of our pulsed positron beam concept was successful.

Finally, fifth chapter demonstrates how positron lifetime beam measurements are used in practice to identify defects in thin layers. Experiments have been performed on InN layers using the pulsed positron lifetime beam facility at Universität der Bundeswehr in Munich. As a result, defects are observed and they are identified as In vacancies by combining information from Doppler broadening and positron lifetime measurements.

References

[1] K. Fallström and T. Laine. *Appl. Surf. Sci.* **149**, 44 – 48 (1999).

[2] K. Saarinen, P. Hautojärvi and C. Corbel. In *Identification of defects in semiconductors*, edited by M. Stavola, Semiconductors & Semimetals #5, pp. 209 – 285. Academic Press, New York (1998).

[3] D. Schödlbauer, P. Sperr, G. Kögel and W. Triftshauser. *Nucl. Instrum. Meth. B* **34**(2), 258 – 268 (1988).

[4] R. Suzuki, Y. Kobayashi, T. Mikado, H. Ohgaki, M. Chiwaki, T. Yamazaki and T. Tomimasu. *Jpn. J. Appl. Phys.* **30**(3B), L532 (1991).

[5] K. Saarinen, J. Nissilä, P. Hautojärvi, J. Likonen, T. Suski, I. Grzegory, B. Lucznik and S. Porowski. *Appl. Phys. Lett.* **75**(16), 2441 – 2443 (1999).

[6] P. J. Schultz and K. G. Lynn. *Rev. Mod. Phys.* **60**(3), 701–780 (1988).

[7] D. Schödlbauer. *Aufbau und inbetriebnahme einer gepulsten positronenquelle für lebensdauermessungen.* Ph.D. thesis, Universität der Bundeswehr München (1987).

[8] D. Passbach. *Konstruktion und Aufbau eines 50 MHz-Bunchers für PLEPS III.* Master's thesis, Universität der Bundeswehr München, Neubiberg (1997).

[9] A. P. Mills Jr. *Appl. Phys.* **22**, 273 – 276 (1980).

[10] R. Suzuki. *New Positron Annihilation Experiments in Solids.* Ph.D. thesis, Electrotechnical Laboratory, Tsukuba, Ibaraki, Japan (1991).

[11] K. G. Lynn, W. E. Frieze and P. J. Schultz. *Phys. Rev. Lett.* **52**(13), 1137 – 1140 (1984).

[12] S. Szpala, M. P. Petkov and K. G. Lynn. *Rev. Sci. Instrum.* **73**(1), 147–55 (2002).

[13] H. Chen, R. Zhang, Y. Li, J. Zhang, Y. C. Wu, T. C. Sandreczki, P. E. Mallon, R. Suzuki, T. Ohdaira, X. Gu, T. Nguyen and Y. C. Jean. *Mater. Sci. Forum* **445 - 446**, 274 – 276 (2004).

[14] A. P. Mills Jr. In *Positron Solid-State Physics, Course LXXXIII*, edited by W. Brandt and A. Dupasquier, International School of Physics "Enrico Fermi", pp. 432 – 509, Amsterdam (1983). IOS Press.

[15] A. P. Mills Jr. In *Atomic, Molecular, and Optical Physics: Charged Particles*, edited by F. B. Dunning and R. G. Huet, volume 29A of *Experimental Methods in the Physical Sciences*, chapter 2, pp. 39 – 68. Academic Press, Inc. (1995).

[16] S. J. Gilbert, C. Kurz, R. G. Greaves and C. M. Surko. *Appl. Phys. Lett.* **70**(15), 1944–6 (1997).

[17] R. G. Greaves and C. M. Surko. *Phys. Rev. Lett.* **85**(9), 1883 – 1886 (2000).

[18] R. G. Greaves and J. M. Moxom. *Mater. Sci. Forum* **445 - 446**, 419 – 423 (2004).

[19] J. Sullivan, L. Barnes, J. Marler, S. Gilbert and C. Surko. *Mater. Sci. Forum* **445 - 446**, 435 – 439 (2004).

[20] S. Y. Liao. *Microwave devices and circuits.* Prentice-Halle, New Jersey, USA, 3rd edition (1990).

[21] D. L. Webster. *J. Appl. Phys* **10**, 501 – 508 (1939).

[22] S. Humphries, Jr. *Charged Particle Beams.* University of New Mexico, Albuquerque, New Mexico, digital edition (2002). Originally published in 1990 by John Wiley and Sons. `http://www.fieldp.com/cpb/cpb.html`

[23] F. J. Lynch, R. N. Lewis, L. M. Bollinger, W. Henning and O. D. Despe. *Nucl. Instrum. Methods* **159**(2-3), 245–63 (1979).

[24] W. Bauer-Kugelmann. *Technische Weiterentwicklungen am gepulsten Positronenstrahlsystem PLEPS.* Ph.D. thesis, Universität der Bundeswehr München (2000).

[25] E. Hamada, N. Oshima, T. Suzuki, H. Kobayashi, K. Kondo, I. Kanazawa and Y. Ito. *Radiat. Phys. Chem.* **58**(5-6), 771–775 (2000).

[26] M. Tashiro, Y. Honda, T. Yamaguchi, P. K. Pujari, N. Kimura, T. Kozawa, G. Isoyama and S. Tagawa. *Radiat. Phys. Chem.* **60**(4-5), 529–533 (2001).

[27] H. Iijima, T. Asonuma, T. Hirose, M. Irako, K. Kadoya, T. Kumita, B. Matsumoto, K. Wada and M. Washio. *Nucl. Instrum. Meth. A* **483**(3), 641–648 (2002).

[28] J. De-Baerdemaeker and C. Dauwe. *Appl.Surf.Sci.* **194**(1-4), 52–55 (2002).

[29] M. Hirose, T. Nakajyo and M. Washio. *Mater. Sci. Forum* **255 - 257**, 674 – 676 (1997).

[30] H. Iijima, T. Asonuma, T. Hirose, M. Irako, K. Kadoya, T. Kumita, B. Matsumoto, K. Wada and M. Washio. *Nucl. Instrum. Meth. A* **483**, 641 – 648 (2002).

[31] V. S. Pandit, P. R. Sarma and R. K. Bhandari. *Nucl. Instrum. Meth. A* **A276**(1-2), 21–4 (1989).

[32] C. Goldstein and A. Laisne. *Nucl. Instrum. Methods* **61**, 221 – 225 (1968).

[33] W. T. Milner. *IEEE T Nucl. Sci.* **ns-26**(1), 1445–1449 (1979).

[34] M. Aksela. *Pulssitetun positronisuihkun lähdealueen magneettikenttien linjaus sekä esikimputtimen testaus.* Special assignment, Helsinki University of Techology, Department of Engineering Physics and Mathematics (1998).

[35] J. Storgårds. *Positronisuihkun kimputinresonaattorin simulointi ja sähköinen testaus.* Special assignment, Helsinki University of Techology, Department of Engineering Physics and Mathematics (1999).

[36] T. Kiviniemi. *Positronisuihkun kimputinresonaattorin suunnittelu ja sähköinen testaus.* Special assignment, Helsinki University of Techology, Department of Engineering Physics and Mathematics (1994).

[37] J. A. Simpson. *Rev. Sci. Instrum.* **32**(12), 1283–1293 (1961).

[38] C. L. Enloe and n. J. R. Shell. *Rev. Sci Instrum.* **63**(2), 1788 – 1791 (1992).

[39] D. A. Dahl. *Simion 6.0 for Windows.* Ion trajectory simulation software.

[40] Tera Analysis ltd. *Quickfield 5.1.* 2D FEM analysis software.

[41] O.-P. Hiironen. *Energiavalitsimen suunnitteleminen pulssitetuun positronisuihkuun.* Special assignment, Helsinki University of Techology, Department of Engineering Physics and Mathematics (1996).

[42] G. R. Massoumi, P. J. Schultz, W. N. Lennard and J. Ociepa. *Nucl. Instrum. Meth. B* **B30**(4), 592–7 (1988).

[43] H. Huomo, R. Jones, J. Hurst, A. Vehanen, J. Throwe, S. G. Usmar and K. Lynn. *Nucl. Instrum. Meth. A* pp. 359–364 (1989).

[44] F. Reurings. *Compact Positron Beam for Investigation of Positron Source and Moderator Characteristics.* Master's thesis, Helsinki University of Techology, Department of Engineering Physics and Mathematics (2005).

[45] F. Tuomisto. *Pulssitetun positronisuihkun rakenteiden suunnittelu, testaus ja dokumentointi - osa I.* Special assignment, Helsinki University of Techology, Department of Engineering Physics and Mathematics (2000).

[46] S. A. Schwarz. *J. Appl. Phys.* **68**(5), 2382–2391 (1990).

[47] W. S. M. Werner, I. S. Tilinin and M. Hayek. *Phys. Rev. B* **50**(7), 4819–4833 (1994).

[48] Y. Suetsugu, M. Tsuchiya, T. Nishidono, N. Kato, N. Satoh, S. Endo and T. Yokoyama. *J. Vac. Sci. Technol. A* **21**(1), 186 – 195 (2003).

[49] J. Oila. *Kiihdytinrakenteen suunnittelu pulssitettua positronisuihkua varten.* Special assignment, Helsinki University of Techology, Department of Engineering Physics and Mathematics (1997).

[50] A. Pelli, A. Laakso, K. Rytsölä and K. Saarinen. *Submitted to Appl. Surf. Sci.* (2005).

[51] P. Kantola. *Pulssitetun positronisuihkun radiotaajuusohjauselektroniikan testaaminen ja kehittäminen.* Special assignment, Helsinki University of Techology, Department of Engineering Physics and Mathematics (2004).

[52] A. Pelli. *Pulssitetun positronisuihkun rakentaminen ja testaus.* Master's thesis, Helsinki University of Techology, Department of Engineering Physics and Mathematics (2002).

[53] F. Reurings. *Pulssitetun positronisuihkun säteilyilmaisemen testaus sekä ilmaisemen magneettisuojan suunnittelu.* Special assignment, Helsinki University of Techology, Department of Engineering Physics and Mathematics (2004).

[54] P. Sperr and G. Kögel. *Mater. Sci. Forum* **255-257**, 109–113 (1997).

[55] V. Y. Davydov, A. A. Klochikhin, V. V. E. R. P. Seisyan, S. V. Ivanov, J. F. F. Bechstedt, H. Harima, J. A. A. V. Mudryi, O. Semchinova and J. Graul. *Phys. Stat. Sol. (b)* **229**, R1 (2002).

[56] J. Wu, W. Walukiewicz, K. M. Yu, J. W. A. III, E. E. Haller, H. Lu, W. J. Schaff, Y. Saito and Y. Nanishi. *Appl. Phys. Lett.* **80**, 3967 (2002).

[57] E. B. Bellotti, B. K. Doshi, K. F. Brennan, J. D. Albrecht and P. P. Ruden. *J. Appl. Phys.* **85**, 916 (1999).

[58] B. E. Foutz, S. K. Leary, M. S. Shur and L. F. Eastman. *J. Appl. Phys.* **85**, 7727 (1999).

[59] C. Stampfl, C. G. V. de Walle, D. Vogel, P. Krüger and J. Pollmann. *Phys. Rev. B* **61**, R7846 (2000).

[60] D. C. Look, H. Lu, W. J. Schaff, J. Jasinski and Z. Liliental-Weber. *Appl. Phys. Lett.* **80**, 258 (2002).

[61] E. A. Davis, S. F. J. Cox, R. L. Lichti and C. G. V. de Walle. *Appl. Phys. Lett.* **82**, 592 (2003).

[62] M. Alatalo, H. Kauppinen, K. Saarinen, M. J. Puska, J. Mäkinen, P. Hautojärvi and R. M. Nieminen. *Phys. Rev. B* **51**, 4176 (1995).

[63] M. Alatalo, B. Barbiellini, M. Hakala, H. Kauppinen, T. Korhonen, M. J. Puska, K. Saarinen, P. Hautojärvi and R. M. Nieminen. *Phys. Rev. B* **54**, 2397 (1996).

[64] K. Saarinen, P. Seppälä, J. Oila, P. Hautojärvi, C. Corbel, O. Briot and R. L. Aulombard. *Appl. Phys. Lett.* **73**, 3253 (1998).